2006

Efficient suspicious region segmentation algorithm for computer aided diagnosis of breast cancer based on tomosynthesis imaging

Ravi K. Samala
University of South Florida

Efficient Suspicious Region Segmentation Algorithm for Computer Aided Diagnosis of Breast Cancer based on Tomosynthesis Imaging

by

Ravi K. Samala

A thesis submitted in partial fulfillment
of the requirements for the degree of
Master of Science in Electrical Engineering
Department of Electrical Engineering
College of Engineering
University of South Florida

Major Professor: Wilfrido A. Moreno, Ph.D.
Wei Qian, Ph.D.
James Leffew, Ph.D.

Date of Approval:
October 18, 2006

Keywords: perona-malik, anisotropic, 3D diffusion, fuzzy c-means, spatial fuzzy c-means

ACKNOWLEDGEMENTS

I would like to express my deepest gratitude to, my supervisor, Dr. Xuejun Sun for giving me the opportunity to work within the Digital Medical Imaging Program, (DMIP), at the Moffitt Research Center, (MRC). Dr. Sun has been a constant guiding force for my research.

I would like to express my gratitude to Dr. Wei Qian. Dr. Qian assumed the responsibility for directing my research efforts during the final phases, which involved the two crucial events of defending my research efforts and the writing of my thesis.

I would like to express my sincere thanks to, my major professor, Dr. Moreno for showing his confidence in me right from the beginning and constantly reminding me of my goals. It was Dr. Wei Qian's and Dr. Moreno's joint efforts that paved the way for the successful completion of my thesis.

Special thanks to Dr. James T. Leffew for volunteering his time and effort to be in my committee and review my thesis.

I thank my colleagues. Anand and Vidhya provided support unselfishly and offered valuable hints. Raghav, Praveen, Ann and Darshan, my friends, provided moral support and were always there for me. I am grateful to Dinesh Divakaran for his encouragement and valuable suggestions throughout my masters' studies at USF.

Last but certainly not least, I thank my parents and my brothers for constantly encouraging me and reminding me that nothing is impossible to achieve.

TABLE OF CONTENTS

LIST OF TABLES

LIST OF FIGURES

LIST OF ABBREVIATIONS

DBT	Digital Breast Tomosynthesis
FFDM	Full-field Digital Mammography
FN	False Negative
FP	False Positive
MGH	Massachusetts General Hospital
BCDDP	Breast Cancer Detection Demonstration Project
MLM	Maximum Likelihood Method
PM	Perona-Malik
FCM	Fuzzy C-means Clustering
SFCM	Spatial Fuzzy C-means Clustering
SDNR	Signal Difference to Noise Ratio
MQSA	Mammography Quality Standards Act
LMLO	Left Medio-Lateral Oblique View
DMIP	Digital Medical Imaging Program
MRC	Moffitt Research Center
CAD	Computer-Aided Diagnosis
ACS	American Cancer Society
NN	Neural Networks
SAA	Shift-and-Add

BP	Back Projection
PDE	Partial Differential Equations
CT	Computed Tomography

EFFICIENT SUSPICIOUS REGION SEGMENTATION ALGORITHM FOR COMPUTER AIDED DIAGNOSIS OF BREAST CANCER BASED ON TOMOSYNTHESIS IMAGING

Ravi K. Samala

ABSTRACT

Computer aided diagnostic tool can aid the radiologist in the early detection of breast cancer. Even though mammography is considered to be the gold standard for breast cancer detection, it is limited by the spatial superposition of tissue. This limitation is the result of a using a two dimensional, (2D), representation of a three dimensional, (3D), structure. The limitation contributes to and results in misclassification of breast cancers. Tomosynthesis is a limited-angle 3D imaging device that overcomes this limitation by representing the breast structure with 3D volumetric data.

This research, on tomosynthesis imaging, was a critical module of a larger research endeavor for the detection of breast cancer. Tomosynthesis is an emerging state-of-the-art 3D imaging technology. The purpose of this research was to develop a tomosynthesis based, efficient suspicious region segmentation, procedure for the breast to enhance the detection and diagnosis of breast cancer. The 3D breast volume is constructed to visualize the 3D structure of the breast region. Advanced image

processing and analysis algorithms were developed to remove out-of-plane artifacts and increase the Signal Difference to Noise Ratio, (SDNR), of tomosynthetic images. Suspicious regions are extracted from the breast volume using efficient and robust clustering algorithms.

A partial differential equation based non-linear diffusion method was modified to include the anisotropic nature of tomosynthesis data in order to filter out the out-of-plane artifacts, which are termed “tomosynthetic noise”, and to smooth the in-plane noise. Fuzzy clustering algorithms were modified to include spatial domain information to segment suspicious regions. A significant improvement was observed, both qualitatively and quantitatively, in segmentation of the filtered data over the non-filtered data. The 3D segmentation system is robust enough to be used for statistical analysis of huge databases.

CHAPTER 1

INTRODUCTION

Breast cancer is the second leading mortality cause in the United States, [ACS 2006]. The key to surviving breast cancer is early detection and treatment, [Yankaskas 2001]. It has been estimated that in 2006, 214,640 new cases of invasive breast cancers will be diagnosed, with 212,920 in women and 1,720 in men. Approximately 40,970 women and 460 men are expected to die of breast cancer in the year 2006. Additionally, 61,980 new cases of in-situ breast cancer are expected to occur in women in 2006 in addition to invasive breast cancer, [CFF 2006]. Excluding cancer related to skin, breast cancer is considered to be the most common cancer and occurs in approximately one in three women in the United States, [ACS 2006]. Digital Breast Tomosynthesis, (DBT), is expected to overcome the inherent limitations of Full-Field Digital Mammography, (FFDM), which uses a 2 dimensional projection of a 3-dimensional object for early cancer diagnosis.

1.1 Motivation

Even though mammography is considered to be the most cost-effective diagnostic method for breast cancer detection, it possesses serious limitations, which arise due to false negative and false positive interpretations. The sensitivity of mammography is affected by the overlapping of dense fibroglandular tissue and parenchyma, which

obscure lesions in dense breasts, [Chan 2005]. The rate of diagnosis of smaller tumors, (≤2.0cm), increased by 2.1% per year from 1988 to 1999 and remained fairly constant. This statistic indicates the need for the replacement of mammography with a better diagnostic method, which can increase the incidence of detection of small tumors.

False Negative Diagnosis

One of the primary reasons for a false negative diagnosis in mammography, which misses breast cancer, is due to the super-imposition of normal breast tissue on the cancerous region. Approximately 30% of breast cancers are missed in conventional mammography, [Yankaskas 2001]. False negatives also occur because of the small size of the cancerous growth.

False Positive, (FP), Diagnosis

False positives result in the classification of normal breast tissue as cancerous because of the spatial super-imposition of tissue. It was reported by Wu et al, at Massachusetts General Hospital, (MGH), that approximately 25% of FPs occurs. Additionally, it has been reported that close to three-fourths of all post-mammogram biopsy results turn out to be benign lesions by Yankaskas. Super-imposition of normal tissue sometimes causes irregular architectural distortion leading to a false classification of breast cancer.

Mammograms do not provide spatial relationship of structures such as location and depth within the breast region. However, tomosynthesis does provide the important spatial relationships. Spatial relationships of tissue structures are important for diagnosis

or analysis of the cancerous region. After 25 years of data collection by the Breast Cancer Detection Demonstration Project, (BCDDP), with 280,000 volunteers, it was concluded that mammograms missed 10% of cancers in women younger than 50 and 5% in women older than 50, [Cunningham 1997**]**. The false negative rate of mammography is approximately 8-10%, which accounts for the improvements in breast cancer diagnosis standards.

Tomosynthesis is the new diagnostic x-ray imaging system, which overcomes the inherent limitation of mammography.

1.2 Thesis Goals

Tomosynthesis slices, obtained from 11 projections over a 50° angle, were reconstructed using the Maximum Likelihood Method, (MLM), to form 40-60 tomosynthesis slices with 0.1mm x 0.1mm x 1mm resolution along X, Y and Z axes. The Z axis represented the in-depth direction and the X and Y axes represented the in-plane resolution. Figure 1.1 presents a block diagram of the effective suspicious region segmentation.

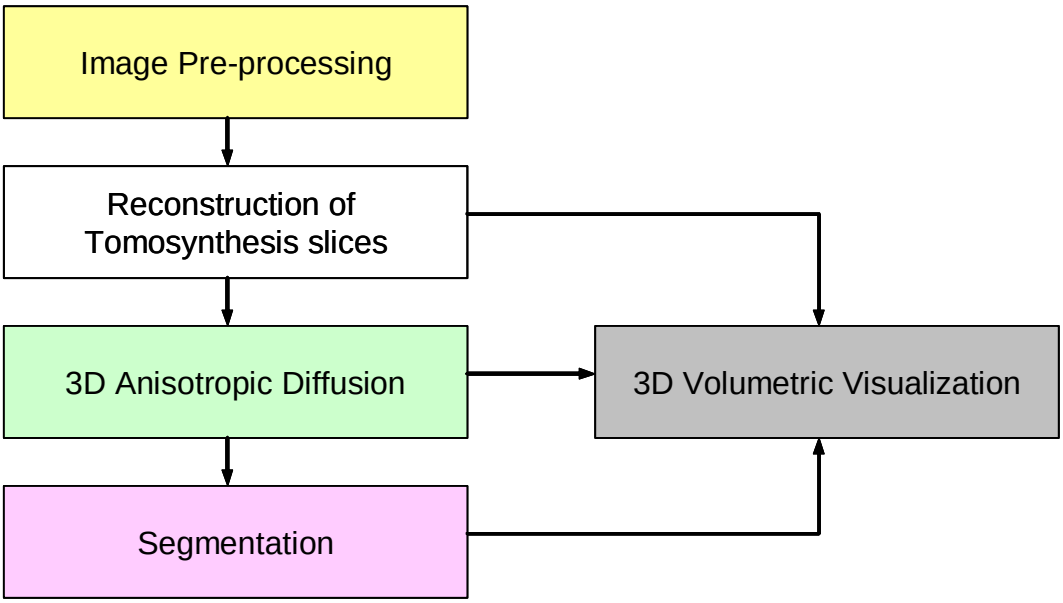

Figure 1.1: Block Diagram of Effective Suspicious Region Segmentation

Perona-Malik anisotropic diffusion was used to filter out the 'tomosynthetic noise' or the structured noise. It was also used to smooth the volumetric image in order to remove noise from the low frequency range. Image pre-processing was performed to remove artifacts and background. In addition, histogram equalization and inversion was used to modify the dynamic range and contrast of the tomosynthesis volume. Segmentation of suspicious regions was achieved using robust fuzzy c-means clustering, (FCM), and spatial fuzzy c-means, (SFCM), clustering.

CHAPTER 2

BREAST CANCER

2.1 Anatomy

The major anatomical structures of the breast are lobules, ducts, connective tissue, fatty tissue and lymphatic tissue. Lobules are where milk producing glands exist and ducts are passages from lobules to the nipple. Breast cancer, which occurs in lobules, is termed "lobular carcinoma in-situ" and breast cancer, which occurs in ducts, is termed "ductal carcinoma in-situ". Figure 2.1 pictures the breast and its anatomical features.

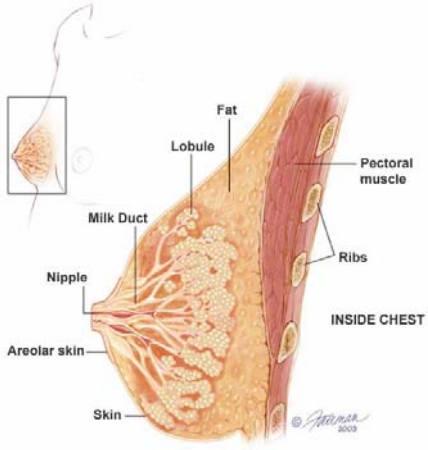

Figure 2.1: Anatomy of the Breast
Source: Massachusetts General Hospital Cancer Resource Room, Boston, MA

Breast cancer is classified as benign, in situ or invasive. The classification depends upon the nature and location of the cancer cells. If the abnormality does not grow uncontrollably then it is benign in nature. In-situ breast cancer is confined within

the lumps or the lobules and has not spread to other areas. Invasive breast cancer is a type that spreads to other areas. Figure 2.2 pictures the areas of the breast where lobular carcinoma and ductal carcinoma originate.

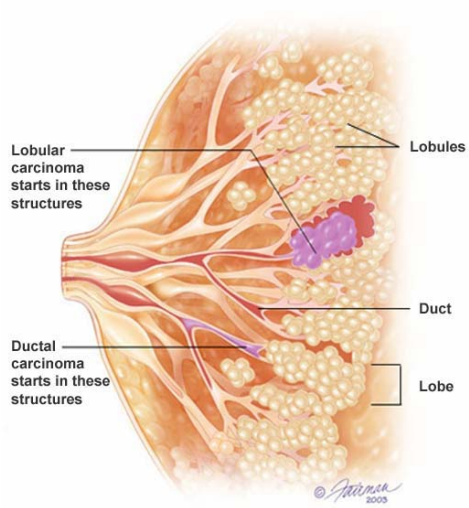

Figure 2.2: Anatomy of the Breast with Lobules and Ducts
Source: Massachusetts General Hospital Cancer Resource Room, Boston, MA

2.2 Breast Cancer Facts

A huge amount of statistical analysis has been performed in the area of breast cancer diagnosis. In particular, the relationship between early diagnosis and survival rate has been analyzed extensively. These analyses have produced critical information. For example:

- It was estimated that in the year 2005, 211,240 new cases of invasive breast cancers, and an estimated 58,490 cases of in-situ breast cancer would be diagnosed in women. Approximately 40,410 women were expected to die of breast cancer in the year 2005, [Imaginis 2006].

- The incidence of breast cancer and the associated mortality rate increases with age. Women over the age of 40 are considered to be highly vulnerable and represent potential candidates for frequent checkup. During 1998 - 2002, 95% of new cases and 97% of deaths associated with breast cancer occurred in women over the age of 40, [ACS 2006].
- The probability of developing invasive breast cancer, within selected age intervals, is presented in Table 2.1[CFF 2006].

Table 2.1: Probability of Invasive Breast Cancer Within Selected Age Intervals

Age Interval	Percentage
Birth – 39	0.48%
40 – 59	4.11%
60 – 69	3.82%
70 – Older	7.13%
Birth – Death	13.22%

- Even though men are considered to be at low risk of acquiring breast cancer, approximately 1690 cases of breast cancer were expected to occur in 2005, which was 1% of all breast cancers in 2005. Approximately 460 men were expected to die of breast cancer in 2005, [ACS 2006].
- Between 1975 and 1990 the death rate increased by 0.4% annually. However, between 1990 and 2002, the death rate decreased by 2.3% annually. The decrease was due to early detection improvements in the treatment of breast cancer.

2.3 Mammography

Mammography is an x-ray imaging device, which uses a rotating anode to project x-rays onto the targeted area. Depending upon the density of the tissue, the absorption of x-rays varies. A detector, which either a screen film or a digital device, is used to capture the x-rays after passing through the target.

Regular mammography screening and follow-up examinations have produced a significant decrease in the mortality due to breast cancer. The principal reason for the death rate decrease is attributed to the early detection of the carcinoma prior to the occurrence of any physical symptoms, [CDC 2005]. With the introduction of mammography from 1980 to 1987, incidence of detection of smaller tumors, ($\leq$2.0cm), more than doubled. During the same time period, the incidence of detection of large tumors, ($\geq$3.0cm), decreased by 27%, this was directly related to earlier detection of the cancer. In-situ breast cancer is considered to be the initial stage of the disease. Detection of the cancer at this stage increases the survival rate. Mammography, as a detection mechanism, has proven to be an effective tool since its introduction in 1980.

Digital mammography, which is also called Full field digital mammography, (FFDM), is different from screen-film mammography. The screen used to capture the x-rays in the screen-film device is replaced by digital detectors, which convert the x-rays into electrical signals in the FFDM device. The electrical signals, of the FFDM device, are converted and saved in digital format. The digitized data can be viewed on a computer or printed on a similar film as that related to screen-film mammography.

2.4 Tomosynthesis

In contrast to Mammography, tomosynthesis is a 3D x-ray imaging system. Typically tomosynthesis acquires 11 projection images over a 50^0 angular range. The imaging system uses an a-Si, (CsI:Tl), flat-panel detector, which possesses an acquisition time of less than 7 seconds. The detector and breast positions are fixed during the image acquisition and while the x-ray source is being rotated.

Mammography is the 2D representation of the 3D breast structure. Tomosynthesis is a 3D, volumetric, representation, which is absent of morphological information. As Dobbins points out, the advantages of tomographic imaging over conventional projection radiography are 3D visualization of anatomical structures and improved contrast of local structures.

Breast tissue is extremely dense, which could obscure a lesion on mammography. The existence of this inherent spatial superposition of tissue in mammograms increases the difficulty for cancer detection. In most cases the tumor does not have a significant difference in intensity, color or texture from the surrounding tissue to be distinguishable. Thus, a lesion could be well hidden within the normal tissue, [Chen 2003]. Figure 2.3 illustrates the difference between the imagery of a lesion produced by mammography and tomosynthesis.

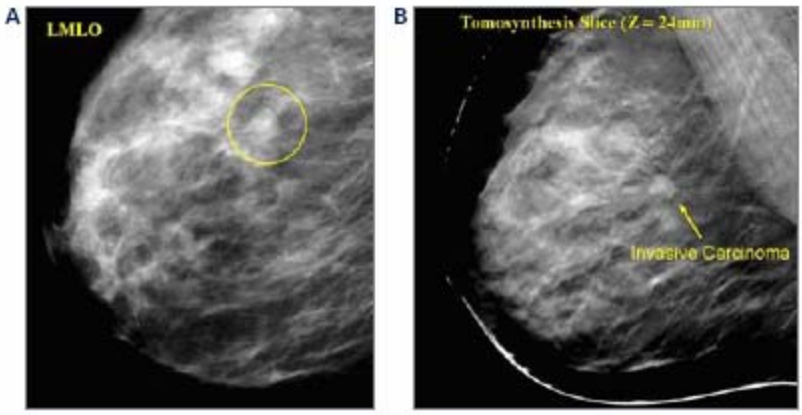

Figure 2.3: A. Standard 2D Left Medio-Lateral Oblique, (LMLO), View with Obscure Lesion. B. Tomosynthesis Slice with Patent Lesion

Photo Courtesy of Mercury Computer Systems Life Sciences.

Even though tomosynthesis was introduced before Computerized Tomography, it did not attract very much attention. Currently, due to advances in x-ray detector devices with respect to large detection area, low noise and fast acquisition time, tomosynthesis has attracted renewed interest.

2.4.1 Acquisition Principal

Tomosynthesis takes advantage of motion parallax. Motion parallax produces an apparent shift in the position of an object against a background as a result of a change in the observer position, [Parallax 2006]. Figure 2.4 illustrates the concept of motion parallax.

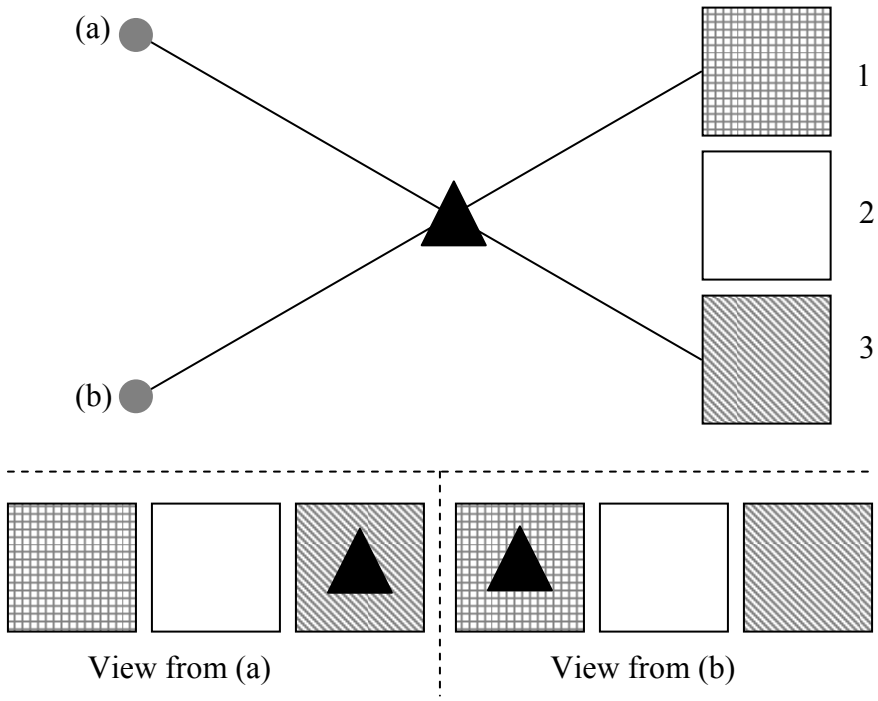

Figure 2.4: Motion Parallax

Viewing from (a) the triangular object appears to be in front of the background 1. However, viewing from (b) the object appears to be in front of background 3.

The image presented in Figure 2.5 illustrates the methodology associated with a tomosynthesis imaging device. Instead of 11 x-ray sources only 3 x-ray sources are considered for simplicity. A basic shift-and-add reconstruction method is used to reconstruct the image at the plane of interest.

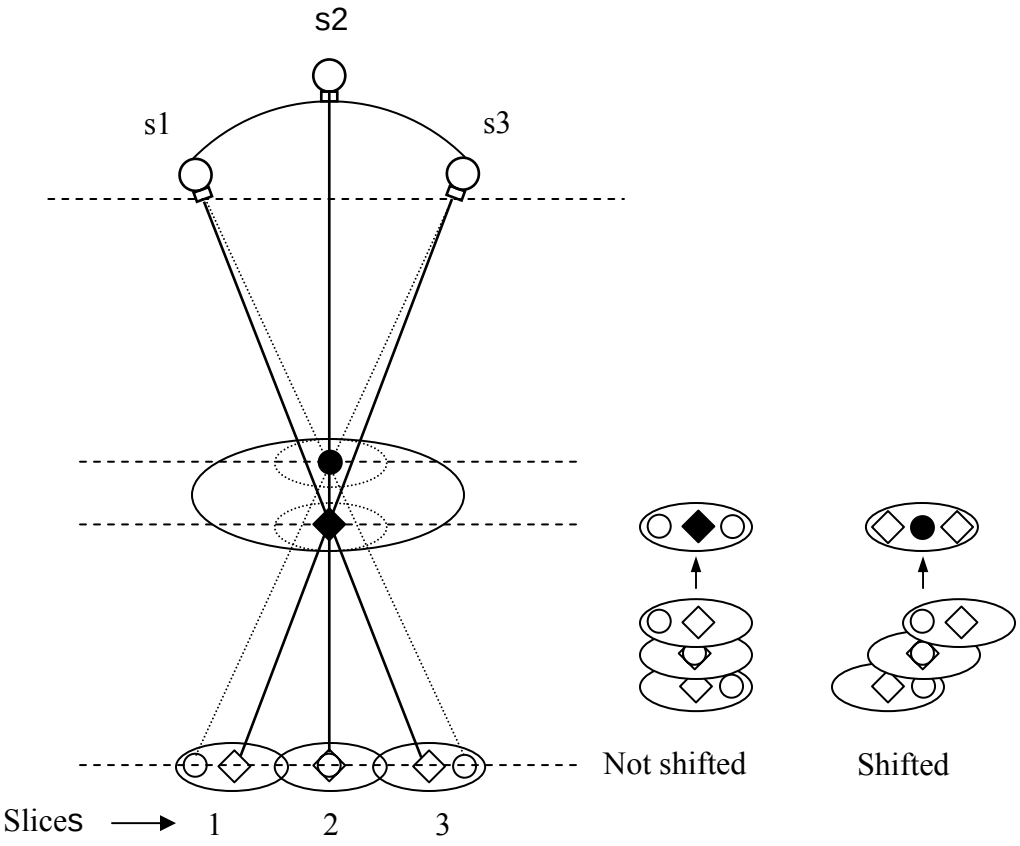

Figure 2.5: Tomosynthesis Acquisition Principal

Even though the in-plane resolution of the reconstructed tomosynthesis volume is comparable with that of mammography, the in-depth resolution is low. Thus the volumetric image is anisotropic in nature.

According to the Mammography Quality Standards Act, (MQSA), regulations, a single view dose of mammography cannot exceed 0.3 rad. The average dose currently used is 1.6 rad. The radiation dose for tomosynthesis images, at each angle, is equal to or slightly greater than the radiation dose associated with standard single-view mammography, [Niklason 1997], [Wu 2003]. The breast is the second most radiosensitive organ in human body, [Rozhkova 2000]. Therefore, radiation dosage level

is an important parameter, which must be considered, when designing a diagnostic imaging device.

CHAPTER 3

BACKGROUND

In the past 15 years, the laboratory at the Moffitt Research Center, (MRC), which is concerned with the Digital Medical Imaging Program, (DMIP), has developed a series of robust procedures. These procedures have been mainly applied for microcalcification cluster detection and mass detection in digital mammograms. Successes associated with the procedures have been demonstrated in many reported clinical evaluations and through the issuance of U.S. Patents, [Qian W. US Patents 1996, 1998a-b, 1999a-b], [Qian, 1993, 1994a-b, 1995a-c, 1996, 1997, 1998a-b, 1999a-b, 2000, 2001, 2002a-b, 2003, 2004 and 2005], [Sun, 2004]. All of research associated with the DMIP forms a strong foundation for the tomosynthesis suspicious region segmentation paradigm.

3.1 Overview of Past Research

The computer-aided diagnosis, (CAD), of mammography, screen film and digital, has been vigorously studied by Dr. Wei Qian and a large number of other investigators over the past decade. The use of current CAD methods for mass detection, when applied to Retrospective Case Analysis, has been widely reported. These methods demonstrate a sensitivity of in the range of 80-90% and an average false positive, (FP), detection rate of (2-4)/image [Petrick 1996, Mendez 1998, Polakowski 1997, Giger 1998]. CAD methods using Retrospective Case studies have proven to be useful for the reduction of the the

variability of reading mammograms when used as a second opinion strategy. The use of current CAD methods for mass detection, when applied to Prospective Case Analysis, have also been studied, Studies of these methods report a significant drop in sensitivity to less than 70% and a similar FP detection rate, [Nishikawa 1998]. However, despite the sensitivity reduction, these methods, when applied to Prospective Case Analysis, have proven to be useful for detection of missed interval cancers. In past years, despite considerable effort by many researchers, the study of CAD procedures has not been able to produce acceptable levels of both detection sensitivity and FP rate for clinical requirements, [Sahiner B., Chan H. P., 1999 and Hadjiiski L. M., 1999]. The drawbacks of CAD methods can be attributed to the lack of a full optimization mechanism. However, a novel, fully automatic and highly efficient method was developed by the MRC during prior research sponsored by the American Cancer Society, (ACS). The ACS sponsored project was concerned with parameter optimization using FROC experiments, which reveals the future of CAD design.

The preliminary work on CAD for the detection and diagnosis of breast cancer was concerned with the search for optimized solutions that have more realistic success in clinical trials. These preliminary efforts focused on iterative and systematic improvements of CAD modules, which employed sound signal processing and engineering principles. Dr. Qian, at the MRC, has developed over several years a novel nonlinear, multistage and adaptive filtering algorithm for image noise suppression and artifact reduction. These types of filtering capabilities are required for implementation of high order wavelet transforms, which are sensitive to noise, [Qian 1993 and 1994a]. Dr. Qian has also employed multi-resolution and multi-orientation wavelets for improved

feature extraction using the unique properties of wavelet transforms. The wavelet transforms were utilized in standard and tree-structured forms, which were implemented on filter banks to preserve image details that inherently allow adaptive approaches, [Qian 1997a, b and 1998a, b]. Additionally, single and multistage Neural Networks, (NN), with significantly increased convergence speed, for more efficient classification and use of features, were investigated as input at different NN stages, [Zheng and Qian, 1994, Qian 2002]. Figure 3.1 presents representative images of the results achieved by the application of a MRC CAD method for analyzing a Spiculated lesion.

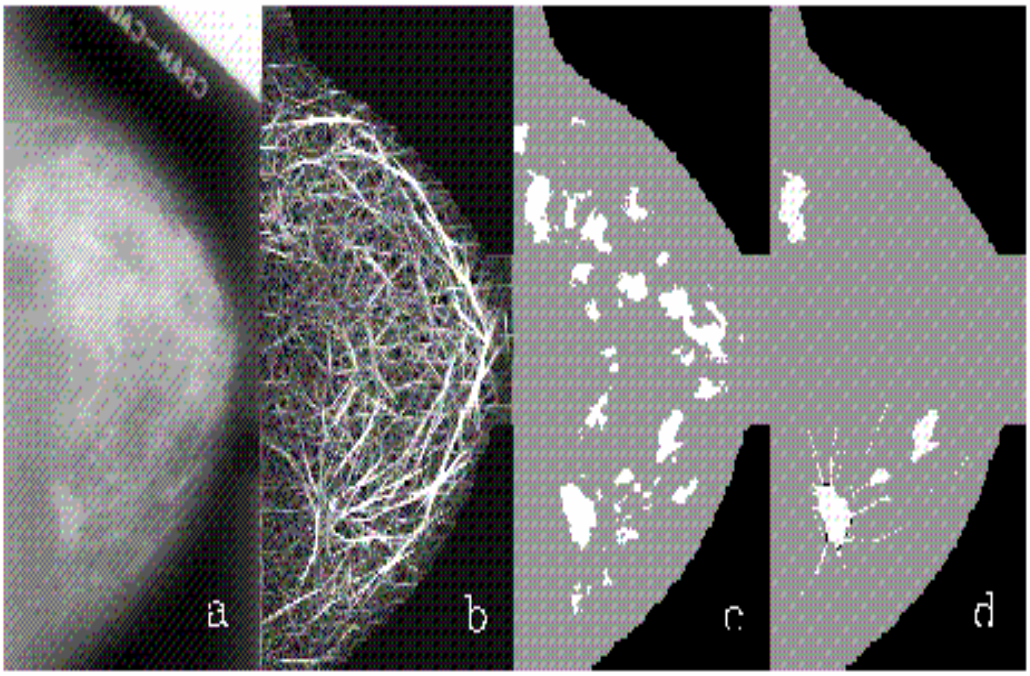

Figure 3.1: Representative Images of a Spiculated Lesion Using a MRC CAD Method

The various images of Figure 3.1 represent:

- a: A raw image at 180μm,
- b: Directional features from a directional wavelet transform, (DWT), using N=8 directions,

- c: segmented image using the multi-resolution tree structured wavelet transform, (TSWT), for enhancement and an adaptive clustering, (AC), module for segmentation of the suspicious area,
- d: Suspicious areas detected with spiculations. An obvious lesion is presented, which allows the shape of the mass and the extent of the spiculation to be visually identified.

The MRC research has been applied to mass detection, which led to the awarding of five United States patents for Dr. Wei Qian and several journal publications and proceedings, [Qian 1993, 1994, 1995, 1996, 1997, 1998, 1999, 2000, 2001 and 2002]. Figure 3.2 presents representative results obtained by applying CAD methods to three Spiculated Lesions with varying levels of subtle and parenchyma tissue density backgrounds.

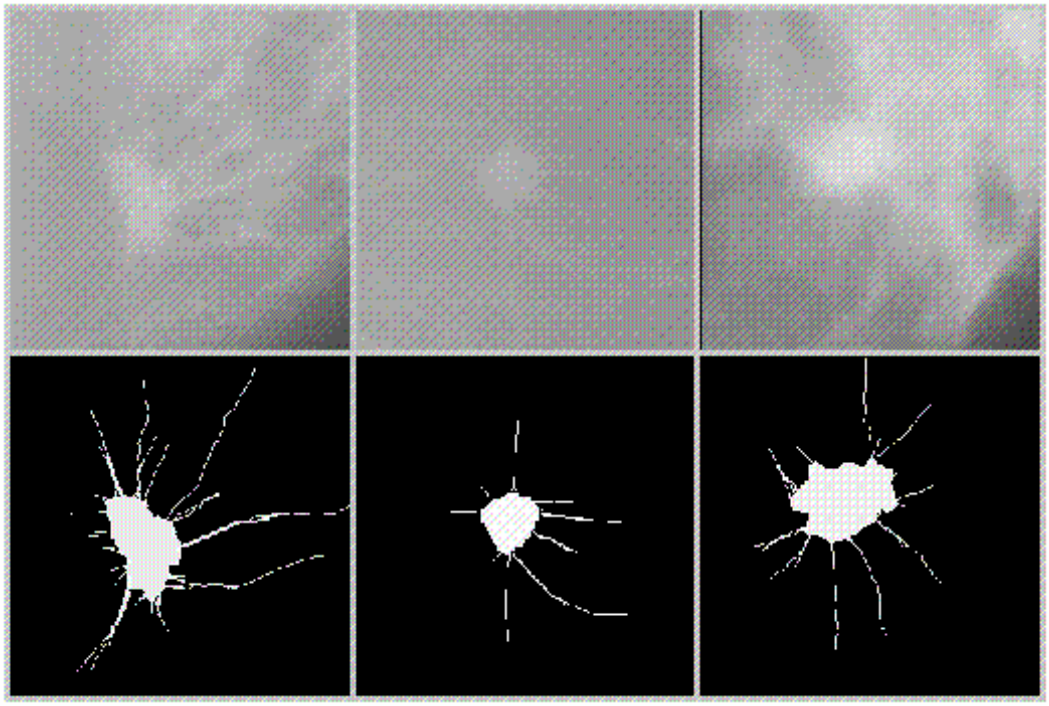

Figure 3.2: Representative Sub-images of Three Spiculated Lesions with Varying Levels of Subtle and Parenchyma Tissue Density Backgrounds

The top row of images in Figure 3.2 presents the raw image data. The bottom row of images in Figure 3.2 presents the segmented lesion with spiculations.

3.2 Filtering

Image processing is generally used to enhance the image for human viewing and to process the image for feature measurement, [Russ 1995]. The current research was more concerned with image enhancement for feature enhancement. Noise can be introduced at image formation, recording or at the transmission stage. Noise is typically present in the form of sharp transitions in the image. Therefore, image smoothing eliminates noise but also introduces blurring, which reduces the contrast of the tissue in the case of medical images. Image enhancement increases the contrast of the images but does not eliminate noise. Therefore, an ideal filtering process must be employed if both image smoothing and enhancement are to be achieved at the same time.

Tomosynthesis is a limited angle image formation technique. Therefore, the most basic reconstruction algorithms of "shift-and-add", (SAA), and "back projection", (BP), suffer from out-of-plane, (OP), artifacts along the depth axis of the tomosynthesis volume. This is an inherent disadvantage of tomosynthesis reconstruction method.

Therefore, objects from other planes get superimposed on the plane of interest after getting blurred out, which results in lower contrast of the objects in the plane of interest. Several methods have been suggested to reduce the impact of this property, [Chakraborty 1984], [Roy 1985], [Badea 1998], [Kim 2005], [Kolitsi 1993]. Badea implemented a wavelet based transformation method to separate noise and in-plane structures and used selective suppression of unwanted structures.

PM diffusion has been used successfully in medical/non-medical imaging fields for noise reduction, image enhancement and segmentation, [Voci 2004], [Gerig 1992]. Gerig discusses the importance of anisotropic filtering of MRI data for reducing the blur of object boundaries and the enhancement of fine structural details.

3.3 Segmentation

One of the primary reasons why FCM was considered to be better than other clustering methods is that one pixel can belong to different clusters at the same time with different degrees. This feature can be exploited to increase the sensitivity of the medical diagnostic system. A number of fuzzy c-means clustering methods were developed with main emphasis placed on modification of the objective function. The objective function was modified to either introduce the spatial information or to use the kernel induced distance metric. FCM with spatial information is less sensitive to noise, [Chuang 2006]. FCM with a kernel induced distance metric, for the objective function, is less sensitive to inhomogeneities in spatial intensity, [Zhang 2004]. Wang implemented a feature-weight learning procedure, which depends on a gradient descent technique to improve the performance of fuzzy c-means clustering.

3.4 Proposed Methodology

Depending on the pixel grey level, directly segmenting the suspicious region gives rise to higher FP detections. Filtering the volumetric data for artifacts removal and image enhancement for better suspicious region segmentation can be achieved through the use of a Perona-Malik, (PM), Anisotropic Diffusion filter. Image processing based on

partial differential equations. A partial differential equation, (PDE), possess the inherent advantage of being easily extended to higher dimensions, allow the use of finite difference methods for solution and provide stable solutions, [Suri 2001]. The breast consists of a complex distribution of tissue. Therefore, a linear filter cannot be used for image enhancement or image restoration. The anisotropic filter is a non-linear filter, which uses the image gradient as the criteria for smoothing or enhancing low, medium and high range frequencies. The anisotropic nature of the volumetric data was considered during the filtering process.

The PM anisotropic diffusion is based on a PDE framework. Therefore, the degree of diffusion can be controlled in any dimension and the control process can be extended to higher dimensions. As a result of this pivotal characteristic, PM diffusion was chosen to smooth tomosynthesis images by removing noise and the blurring along the in-depth direction. PM diffusion was also utilized to enhance images of tissue structures.

The use of a Perona-Malik anisotropic diffusion filter encourages intra-region smoothing while inhibiting inter-region smoothing. PM diffusion satisfies the basic requirement of filtering medical data. These requirements consist of actions to:

- Preserve object boundaries and detail structures,
- Remove noise in the regions of homogeneous physical properties.

Figure 3.3 presents plots of the diffusion coefficient with respect to the ratio of the the Gradient and K.

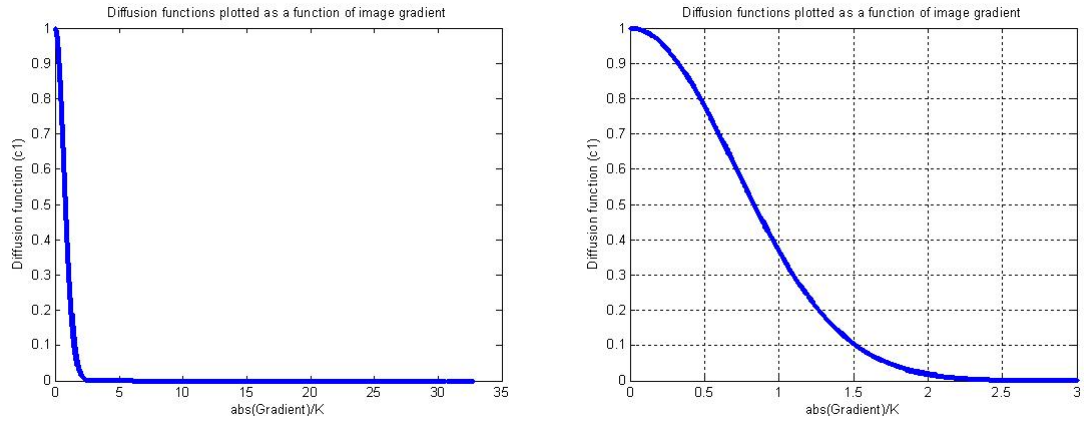

Figure 3.3: Plots of the Diffusion Coefficient with Respect to the Ratio of the Gradient and K

Figure 3.4 presents plots of the flow function with respect to the ratio of the Gradient and K.

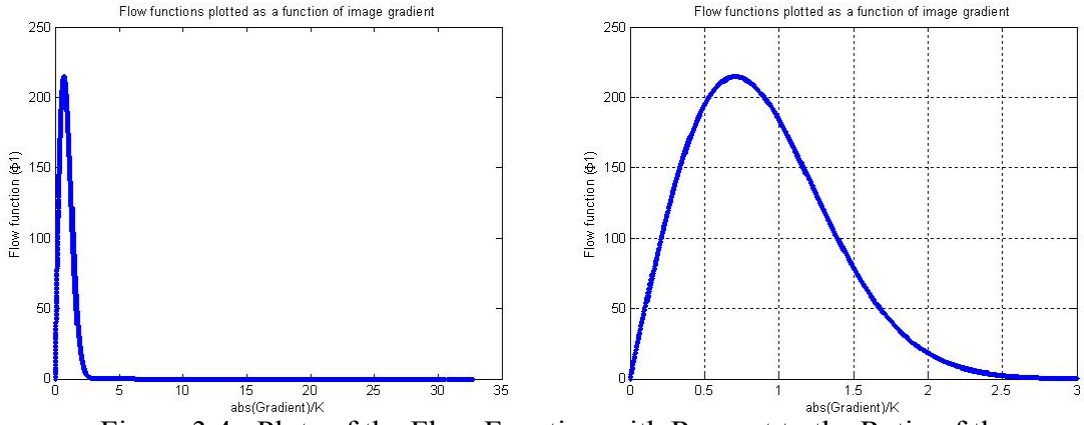

Figure 3.4: Plots of the Flow Function with Respect to the Ratio of the Gradient and K

The plots of Figures 3.3 and 3.4 are typical PM Anisotropic Filtering Curves.

The process is defined in Equation 1 by:

$$\frac{\partial}{\partial t} I(\bar{x},t) = \nabla \bullet (\lambda(\bar{x},t) \nabla I(\bar{x},t)) \qquad (1)$$

Where, $I(\bar{x},t)$ is the tomosynthesis image, $\bar{x}$ is the image axis and *t* refers to the iteration step. The function, $\lambda(\bar{x},t)$, refers to the diffusion function, which is defined as a function of the image gradient by:

$$\lambda(\bar{x},t) = f(|\nabla I(\bar{x},t)|). \tag{2}$$

The diffusion function:

$$\lambda\ (\bar{x},t) = \exp\left(-\left(\frac{|\nabla I(\bar{x},t)|}{K}\right)^2\right) \tag{3}$$

The parameter, *K*, is defined as the diffusion constant and the behavior of the filter depends upon the value of *K*. The value of *K*, determines the amount of smoothing that can be controlled. The flow function is defined as:

$$\Phi(\bar{x},t) = \lambda(x,t) \cdot \nabla I(\bar{x},t). \tag{4}$$

Hence,

$$\frac{\partial}{\partial t} I(\bar{x},t) = \nabla \bullet (\Phi(\bar{x},t)). \tag{5}$$

A 3 dimensional based anisotropic diffusion equation can be written as:

$$\begin{aligned}\frac{\partial I(x,y,z,t)}{\partial t} &= div[\lambda(x,y,z,t)] \\ &= \frac{\partial}{\partial x}[\lambda(x,y,z,t)\frac{\partial I(x,y,z,t)}{\partial x}] + \frac{\partial}{\partial y}[\lambda(x,y,z,t)\frac{\partial I(x,y,z,t)}{\partial y}] + \\ &= \frac{\partial}{\partial z}[\lambda(x,y,z,t)\frac{\partial I(x,y,z,t)}{\partial z}]\end{aligned} \quad . \quad (6)$$

In an 8–1–1 diffusion configuration, 8 pixels are used from the in-plane slice, 1 pixel is used from the top slice and 1 pixel is used from the bottom slice. The calculation is defined by:

$$\begin{aligned}I(x,y,z,t+1) = I(x,y,z,t) + \Delta t\,[&\frac{1}{\Delta}\left(\Phi_{east} + \Phi_{west} + \Phi_{north} + \Phi_{south}\right) + \\ &\frac{1}{\Delta d}\left(\Phi_{northeast} + \Phi_{northwest} + \Phi_{southeast} + \Phi_{southwest}\right) + \frac{1}{\Delta z}\left(\Phi_{top} + \Phi_{bottom}\right)]\end{aligned}, \quad (7)$$

where, Δ is the horizontal or vertical distance between the pixels. Diagonal distance is given by:

$$\Delta d = \sqrt{(\Delta x)^2 + (\Delta y)^2} = \sqrt{2}\Delta \quad (8)$$

and the in-depth distance, Δz, depends on the resolution along the in-depth direction. The calculations for the various cardinal and inter-cardinal directions as well as the top

and bottom calculations are defined by Equations 10, 11 and 12 respectively. These equations are given by

$$\begin{aligned}
\Phi_{east} &= \frac{1}{\Delta x}\left[\lambda(x+\frac{1}{2},y,z,t)\cdot(I(x+1,y,z,t)-I(x,y,z,t))\right] \\
\Phi_{west} &= \frac{1}{\Delta x}\left[\lambda(x-\frac{1}{2},y,z,t)\cdot(I(x-1,y,z,t)-I(x,y,z,t))\right] \\
\Phi_{north} &= \frac{1}{\Delta y}\left[\lambda(x,y-\frac{1}{2},z,t)\cdot(I(x,y-1,z,t)-I(x,y,z,t))\right] \\
\Phi_{south} &= \frac{1}{\Delta y}\left[\lambda(x,y+\frac{1}{2},z,t)\cdot(I(x,y+1,z,t)-I(x,y,z,t))\right]
\end{aligned}, \tag{9}$$

$$\begin{aligned}
\Phi_{northeast} &= \frac{1}{\Delta d}\left[\lambda(x+\frac{1}{2},y-\frac{1}{2},z,t)\cdot(I(x+1,y-1,z,t)-I(x,y,z,t))\right] \\
\Phi_{northwest} &= \frac{1}{\Delta d}\left[\lambda(x-\frac{1}{2},y-\frac{1}{2},z,t)\cdot(I(x-1,y-1,z,t)-I(x,y,z,t))\right] \\
\Phi_{southeast} &= \frac{1}{\Delta d}\left[\lambda(x+\frac{1}{2},y+\frac{1}{2},z,t)\cdot(I(x+1,y+1,z,t)-I(x,y,z,t))\right] \\
\Phi_{southwest} &= \frac{1}{\Delta d}\left[\lambda(x-\frac{1}{2},y+\frac{1}{2},z,t)\cdot(I(x-1,y+1,z,t)-I(x,y,z,t))\right]
\end{aligned}, \tag{10}$$

$$\begin{aligned}
\Phi_{top} &= \frac{1}{\Delta z}\left[\lambda(x,y,z-\frac{1}{2},t)\cdot(I(x,y,z-1,t)-I(x,y,z,t))\right] \\
\Phi_{bottom} &= \frac{1}{\Delta z}\left[\lambda(x,y,z+\frac{1}{2},t)\cdot(I(x,y,z+1,t)-I(x,y,z,t))\right]
\end{aligned}. \tag{11}$$

Suspicious regions were extracted through fuzzy clustering, which depends on the pixel grey level. Further clustering improvement was achieved by introducing a spatial factor. Spatial Fuzzy C-Means, (SFCM), uses information from both the feature and

spectral domains. The use of data from two domains provides an ability to achieve a reduction in sensitivity to noise and better clustering.

CHAPTER 4

FILTERING

Tomosynthesis is a limited-range 3D imaging modality system, which is different from a complete 3D imaging system such as Computed Tomography. Tomosynthesis possesses a limited angular range. Therefore, a slice at a particular focal point of interest is constructed by blurring out-of-plane structures and keeping the in-plane structures intact along the in-depth direction of the volumetric data. The out-of-plane artifacts are inherent and must be removed before segmentation to avoid false positive detections.

4.1 Image Pre-processing

The objective of image pre-processing is to remove unwanted artifacts and enhance the image for further image processing. Image pre-processing is applied prior to filtering the tomosynthesis data for blurring and noise removal.

4.1.1 Background and Artifact Removal

Tomosynthesis results in 14-bit, grey level, images. The dynamic range of the image encompasses $(0 – (2^{14} – 1))$ or (0 – 16,383). However, a limited dynamic grey level range is used for the breast region. The limited dynamic range for the breast region is necessary due to the presence of artifact and background regions, which result in lower

contrast. Figure 4.1, presents a typical tomosynthesis slice with image, artifacts, background and breast region along with the histogram spread.

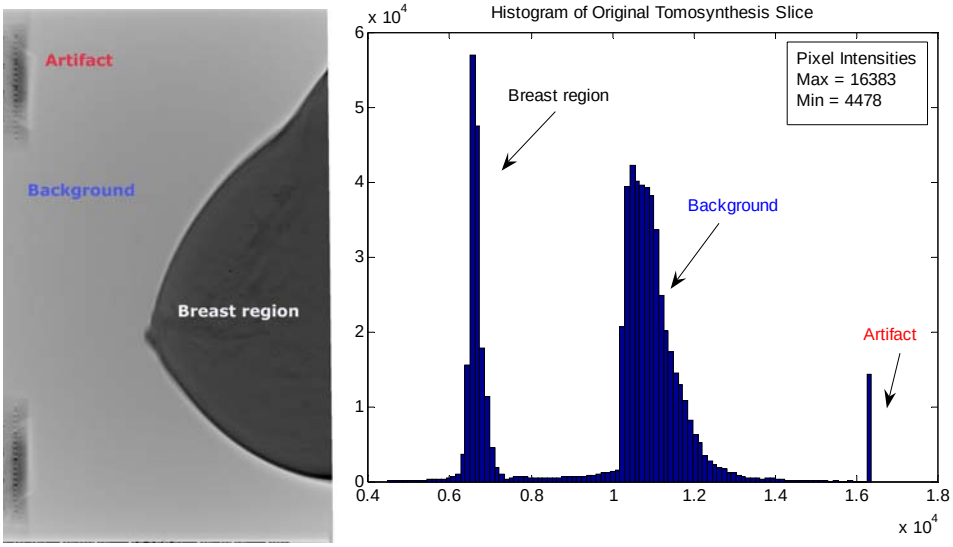

(a) (b)

Figure 4.1: (a) Typical Tomosynthesis Slice
(b) Histogram

Two edge-detection methods were used to extract the breast region, which is the region of interest. The canny edge detection method combines Gaussian smoothing, gradient calculation and a non-maximum suppression technique followed by hysteresis to detect the breast region edge. The other edge detection method utilized was fuzzy c-means, (FCM), clustering. In FCM the number of clusters was chosen as a function of the histogram spread. Figure 4.2 presents a comparison of both edge-detection methods. FCM clustering provided a better classification of the breast region than the canny edge detection method.

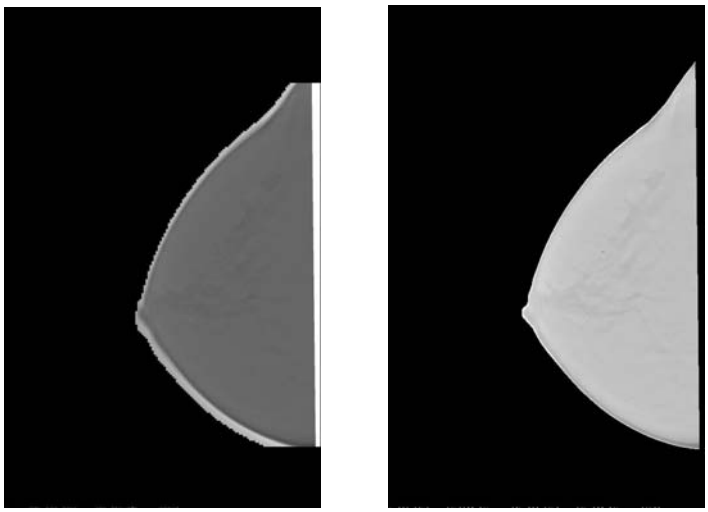

(a) (b)

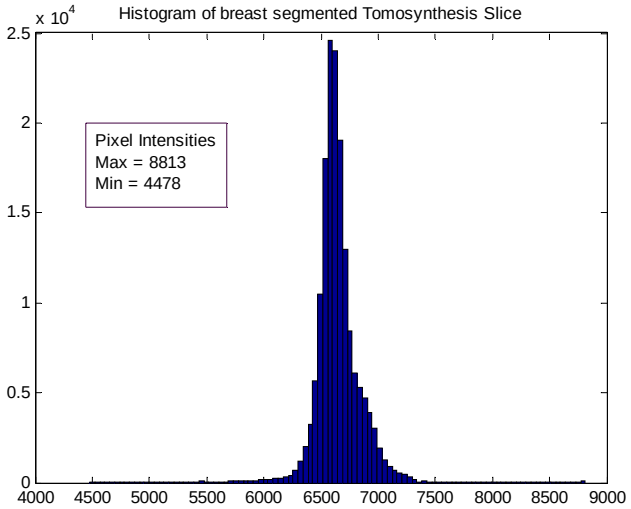

(c)

Figure 4.2: Segmentation of the Breast Region Using
(a) Canny Edge Detection
(b) Fuzzy C-means Clustering
(c) Histogram of the Segmented
Tomosynthesis Slice of the Breast

In order to emphasize the advantages of tomosynthesis imaging it is useful to observe the 3D tomosynthesis volume before and after breast segmentation. Figure 4.3 presents the 3D tomosynthesis volume before and after breast segmentation

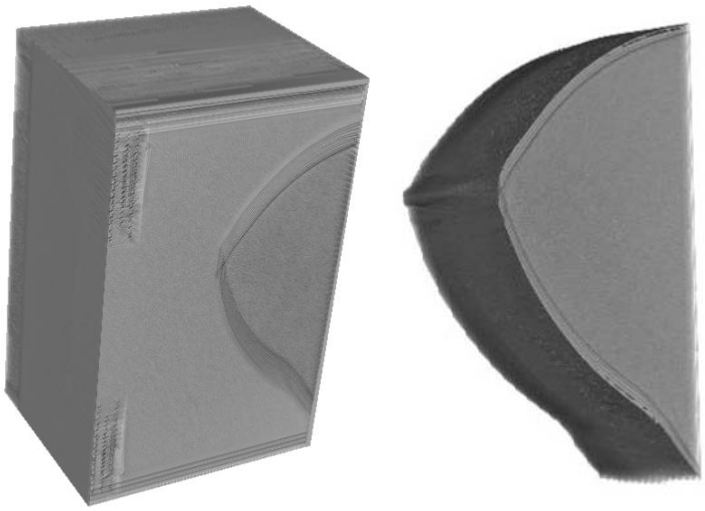

(a) (b)

Figure 4.3: 3D Tomosynthesis Volume Views
(a) Breast Volume with Artifacts and Background
(b) Breast Volume After Removal of the
Artifacts and Background

4.1.2 Inversing

The objective of inversing the image is to shift the histogram of the image to the right side, which is in the direction of a higher dynamic range. Figure 4.4 presents an image of the inversed segmented breast slice and the resulting histogram. A comparison of Figures 4.2 and 4.4 clearly depicts the movement of the histogram to a higher dynamic range.

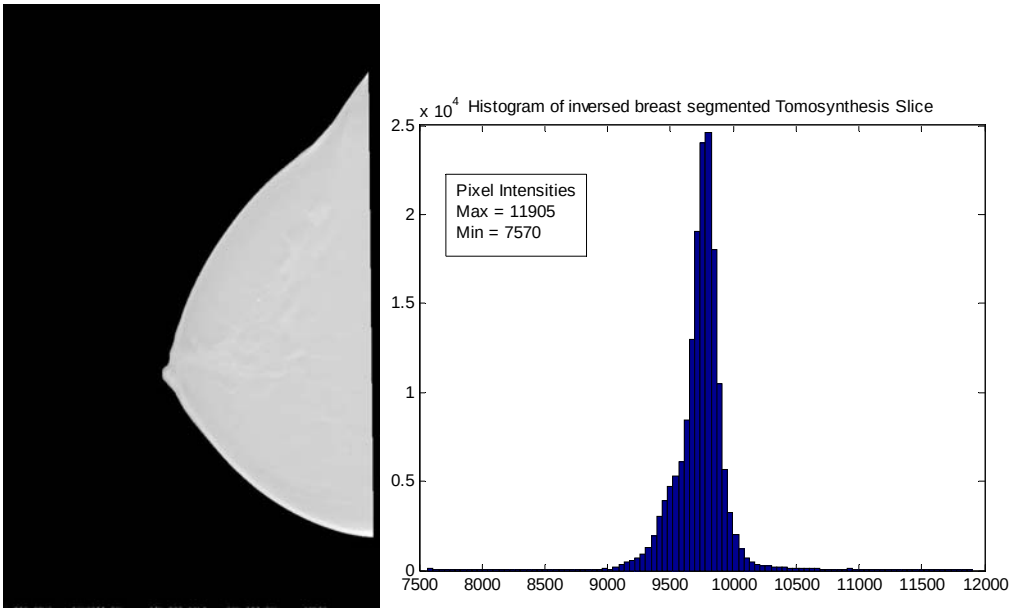

(a) (b)

Figure 4.4: (a) Inversed Segmented Tomosynthesis Breast Slice
(b) Histogram

4.1.3 Histogram Equalization

Histogram equalization enhances the contrast of the tissue structure and aids in improved segmentation. In the inversed image the pixel range was (7,570 – 11,905). The actual image pixel range was (0 – 16383), which encompassed the entire available dynamic range of the 14 bit image. Figure 4.5 presents the inversed, equalized histogram, segmented breast slice and equalized histogram.

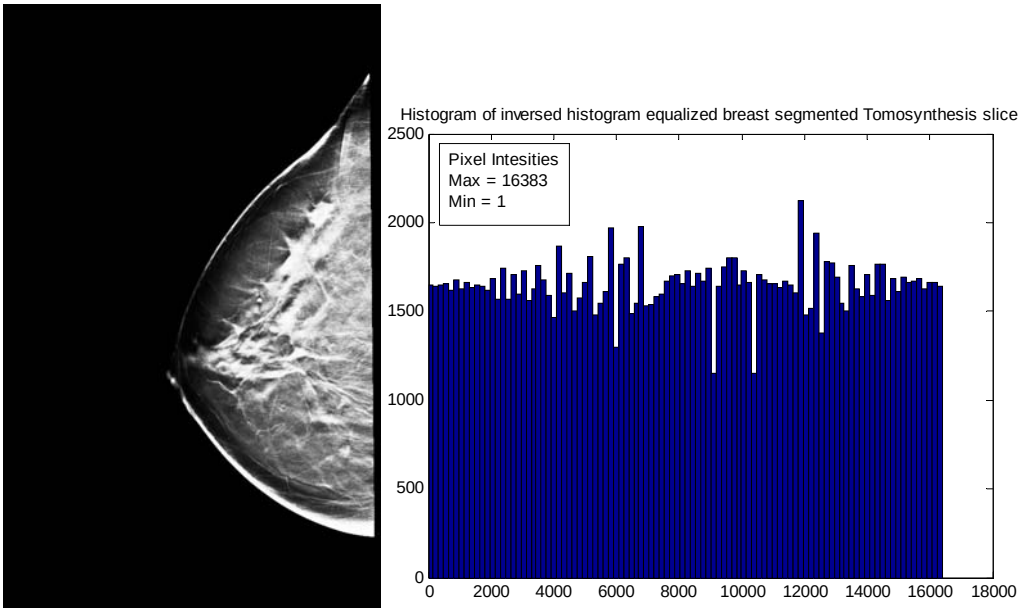

(a) (b)

Figure 4.5: (a) Histogram Equalized Inversed Segmented Tomosynthesis Breast Slice
(b) Equalized Histogram

A comparison of Figure 4.4(a) and Figure 4.5(a) reveals that, after equalization, the structural detail can be seen more clearly.

4.2 Perona-Malik, (PM), Anisotropic Filtering

It was pointed out in section 3.4 that PM diffusion can be extended to higher dimensions. In addition, the anisotropic nature of the data can be included in the filtering process. Different 2D and 3D windows were tested to compare and establish an efficient window to remove out-of-plane artifacts. Experiments with the various windows were required in order to establish appropriate values for the *K* parameter and the learning coefficient, λ.

4.2.1 Choosing the Value of the Learning Coefficient, (λ)

The stability of the filter and the rate at which diffusion is performed is controlled by the learning coefficient, (λ). In order to evaluate the best suitable value, for the learning coefficient, for tomosynthesis data, filtering was performed on a phantom while the value of K and the number of iterations was held constant. The images and the line profile for the chosen Region of Interest, (ROI), is presented in Figure 4.6.

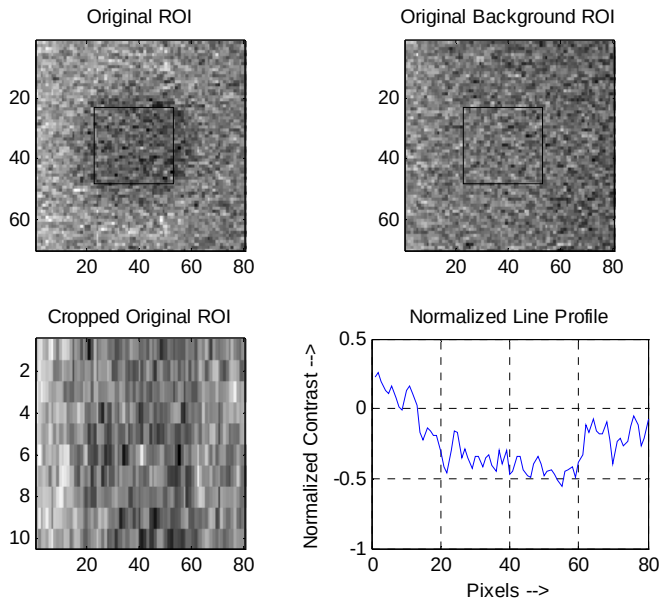

Figure 4.6: Images and Normalized Line Profile for the Chosen ROI with the Iterations = 500 and *K* = 500

The value of K and the number of iterations was maintained at 500. The value chosen for the learning coefficient was varied. The values chosen for the learning coefficient were 0.01, 0.05, 0.1, 0.15 and 0.2. Four, (4), adjacent pixels were chosen in the filtering process. In order to construct the line-profile, the average background pixel intensity was subtracted from the ROI, [Wu 2004]. Ten consecutive rows, with 60 pixels per row, were averaged. The profile was then divided by the number of pixels. The

results for the images and line profile of the ROI for the various values of the learning coefficient are presented in Figures 4.7, 4.8, 4.9, 4.10 and 4.11.

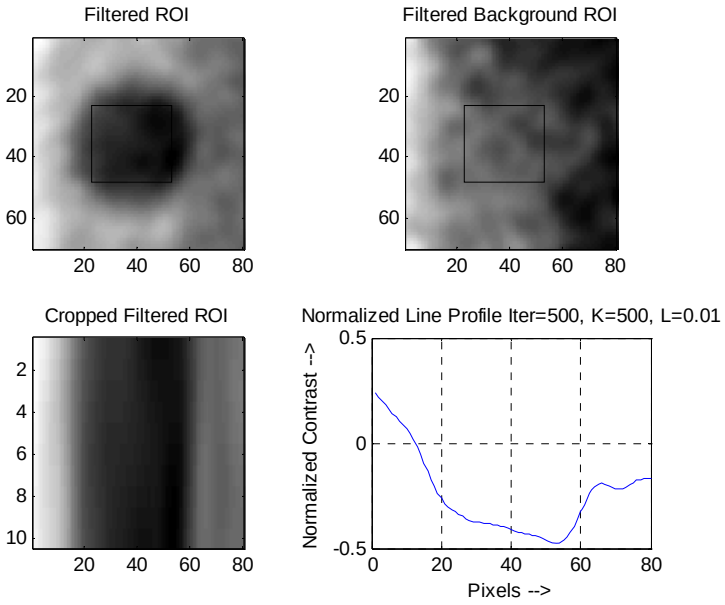

Figure 4.7: Images and Line Profile of the ROI for $\lambda = 0.01$

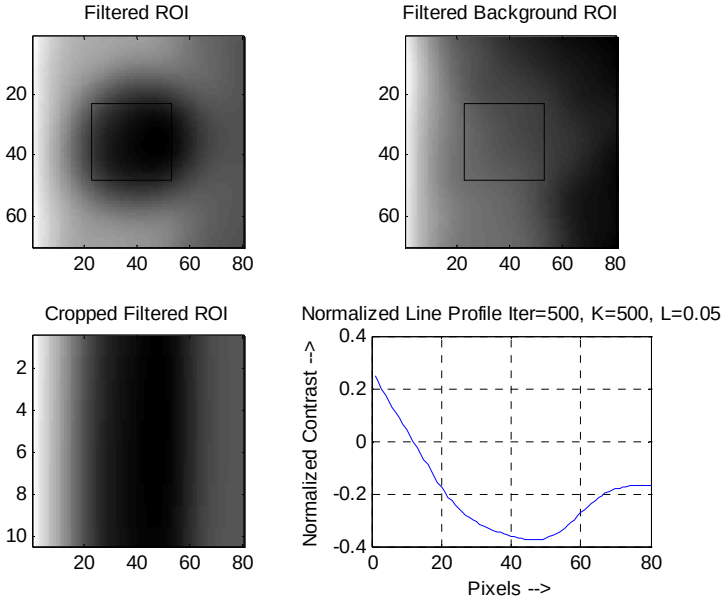

Figure 4.8: Images and Line Profile of the ROI for $\lambda = 0.05$

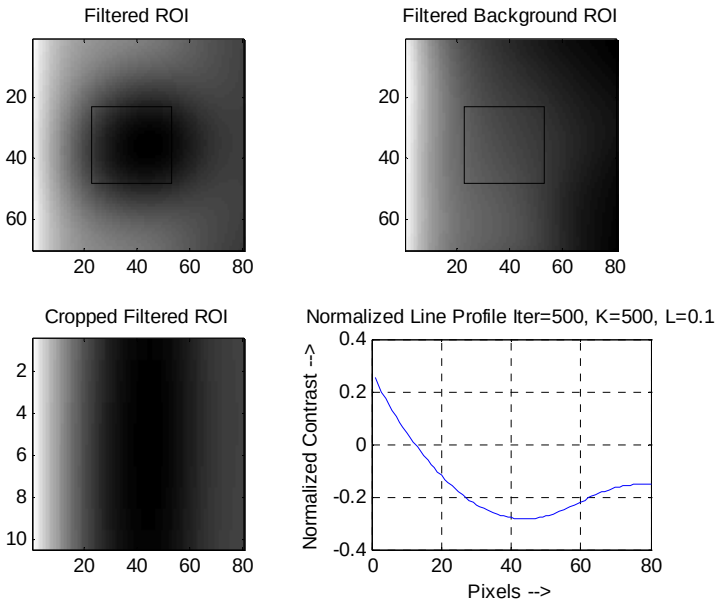

Figure 4.9: Images and Line Profile of the ROI for $\lambda = 0.1$

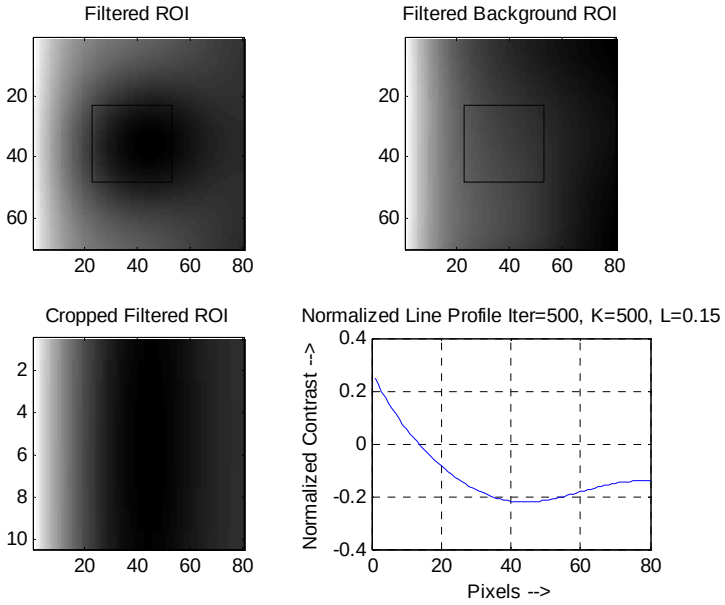

Figure 4.10: Images and Line Profile of the ROI for $\lambda = 0.15$

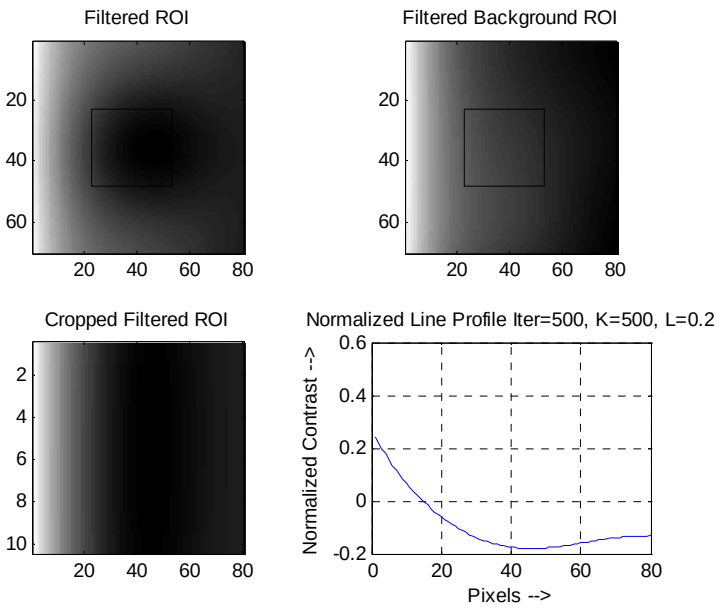

Figure 4.11: Images and Line Profile of the ROI for λ = 0.2

A learning curve value for λ of 0.05 yielded the largest normalized contrast range. This result is displayed in Figure 4.8.

The Signal Difference to Noise Ratio, (SDNR), which was introduced by Wu, yields a measure for the ability to detect a feature in the reconstructed plane. The in-plane resolution of a tomosynthesis slice can be evaluated using the SDNR. The SDNR is evaluated in Equation 1 by:

$$SDNR = \frac{\left(\mu_{feature} - \mu_{BG} \right)}{\sigma_{BG}}, \qquad (1)$$

where, $\mu_{feature}$ is the average pixel intensity of the feature, μ_{BG} is the average intensity of the background region and σ_{BG} is the standard deviation of the background pixel intensity. Figure 4.12 presents a histogram of the variation of the SDNR with respect to λ.

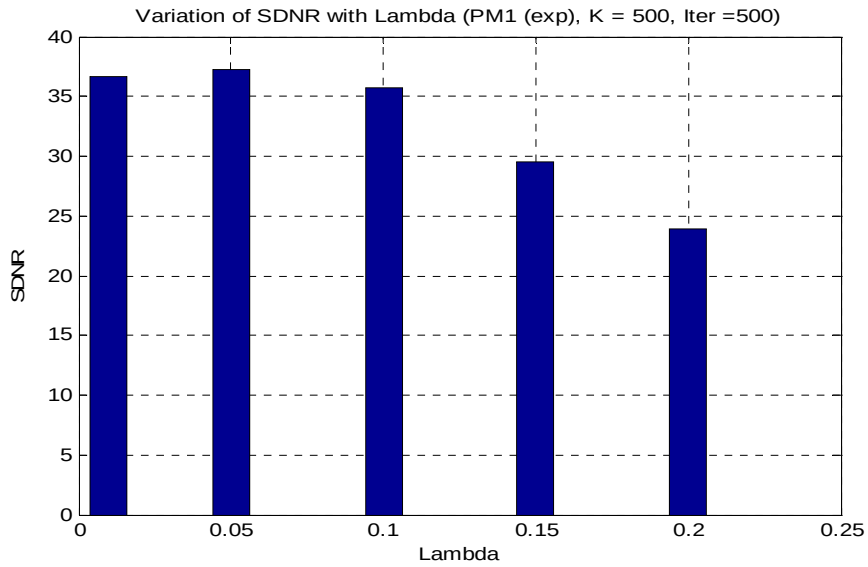

Figure 4.12: Variation of the SDNR with λ

The best SDNR was achieved with a value for the learning coefficient λ of 0.05. Qualitatively, from Figures 4.6 – 4.11, and quantitatively, from Figure 4.12, the best value for the learning coefficient was 0.05. When λ = 0.05, better contrast was observed between the sphere and the background and the highest SDNR was achieved.

4.2.2 Choosing the Value for K

The magnitude of the flow function is highest when the image gradient is close to the value of K. Therefore, it is important, when choosing the optimum value of K, to choose a value that corresponds closely to the gradient values of the out-of-plane

artifacts. Both tomosynthesis phantom and breast data were used to evaluate the value of K. The results for the phantom data investigations are presented in Figures 4.13 – 4.15.

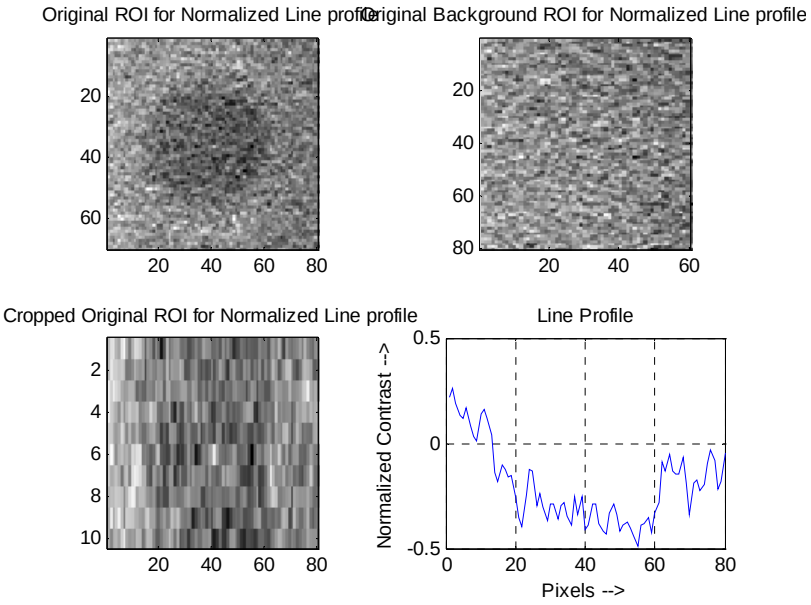

Figure 4.13: Images and Normalized Line Profile for the Chosen ROI with the Iterations = 50 and L = 0.01

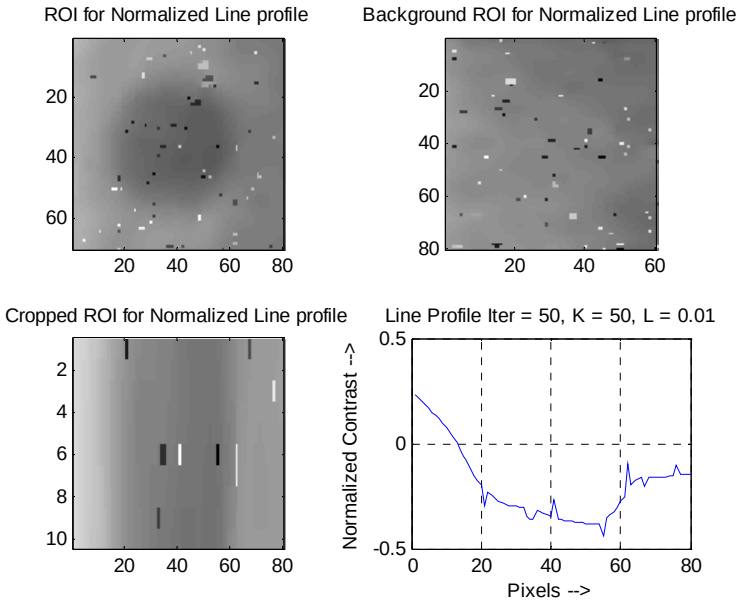

Figure 4.14: Images and Normalized Line Profile for the Chosen ROI with the Iterations = 50, L = 0.01 and *K* = 50

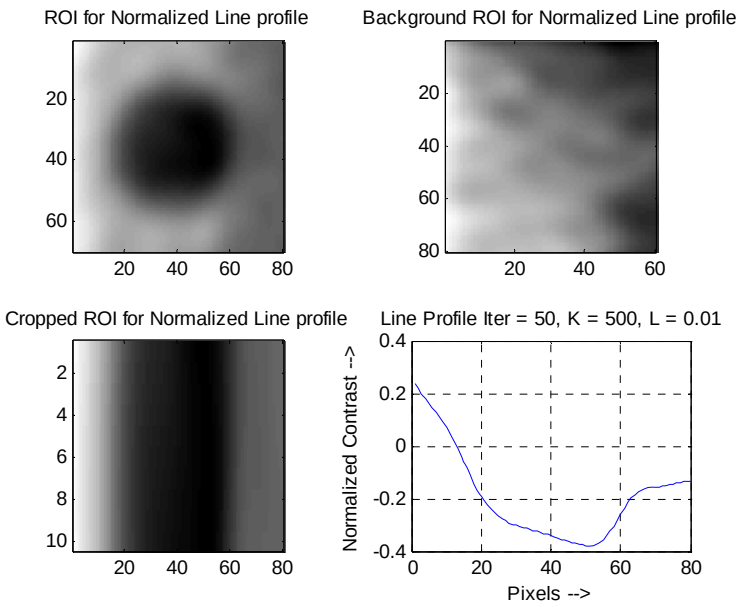

Figure 4.15: Images and Normalized Line Profile for the Chosen ROI with the Iterations = 50, L = 0.01 and *K* = 500

Based on the data presented in Figures 4.13 – 4.15 the best value for *K* is 500.

The results for the breast data investigations are presented in Figures 4.16 – 4.20

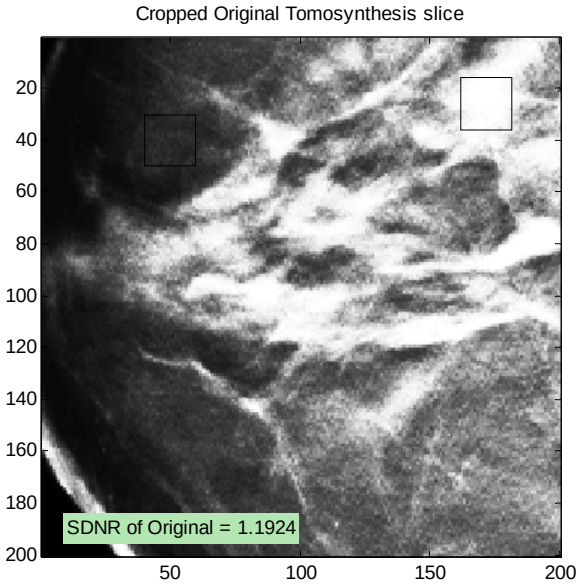

Figure 4.16: Tomosynthesis Breast Slice Chosen for the Investigation of the Optimum Value for *K*

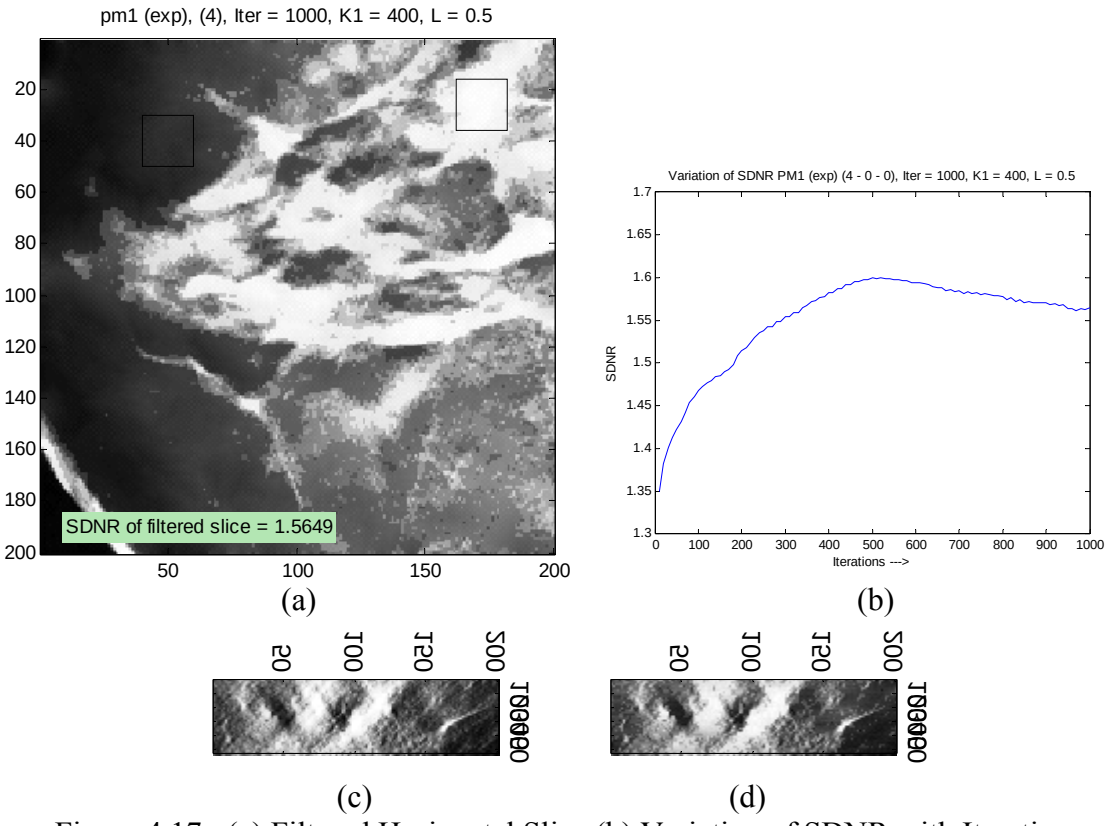

(a) (b)

(c) (d)

Figure 4.17: (a) Filtered Horizontal Slice (b) Variation of SDNR with Iterations (c) Original Vertical Slice (d) Filtered Image of the Original Vertical Slice Iterations = 500, L = 0.5, K = 400

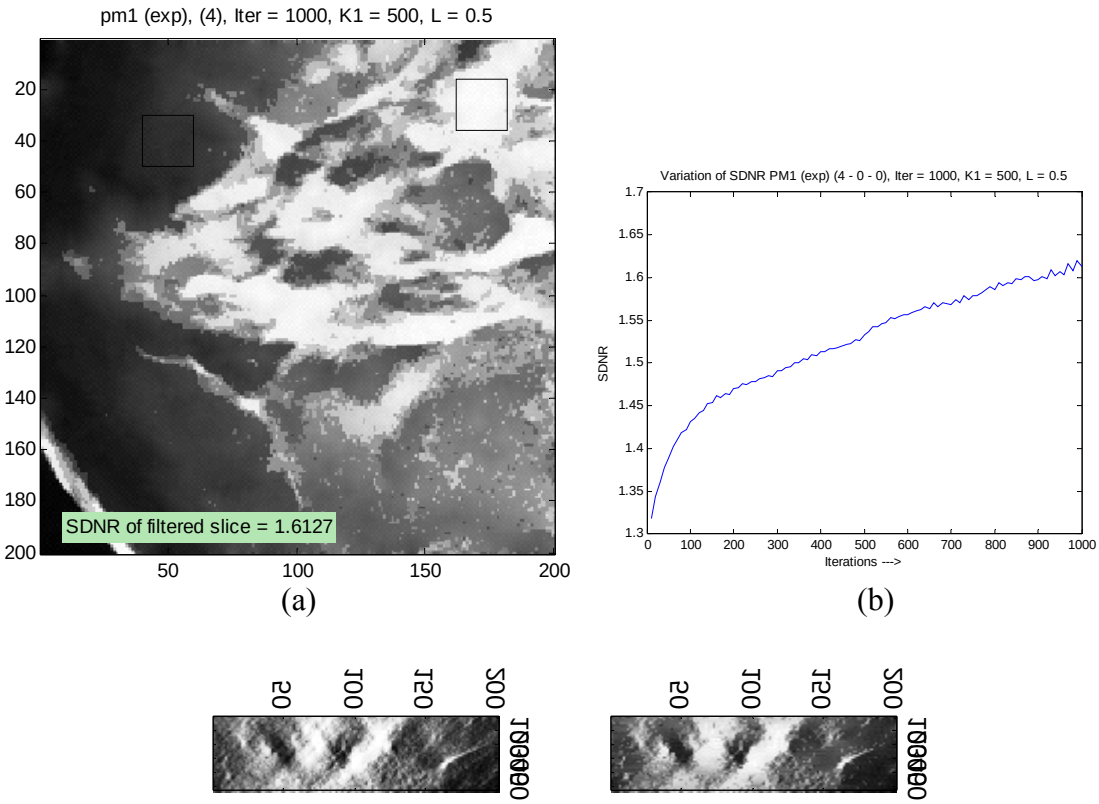

(a) (b)

(c) (d)

Figure 4.18: (a) Filtered Horizontal Slice (b) Variation of SDNR with Iterations (c) Original Vertical Slice (d) Filtered Image of the Original Vertical Slice Iterations = 500, L = 0.5, K = 500

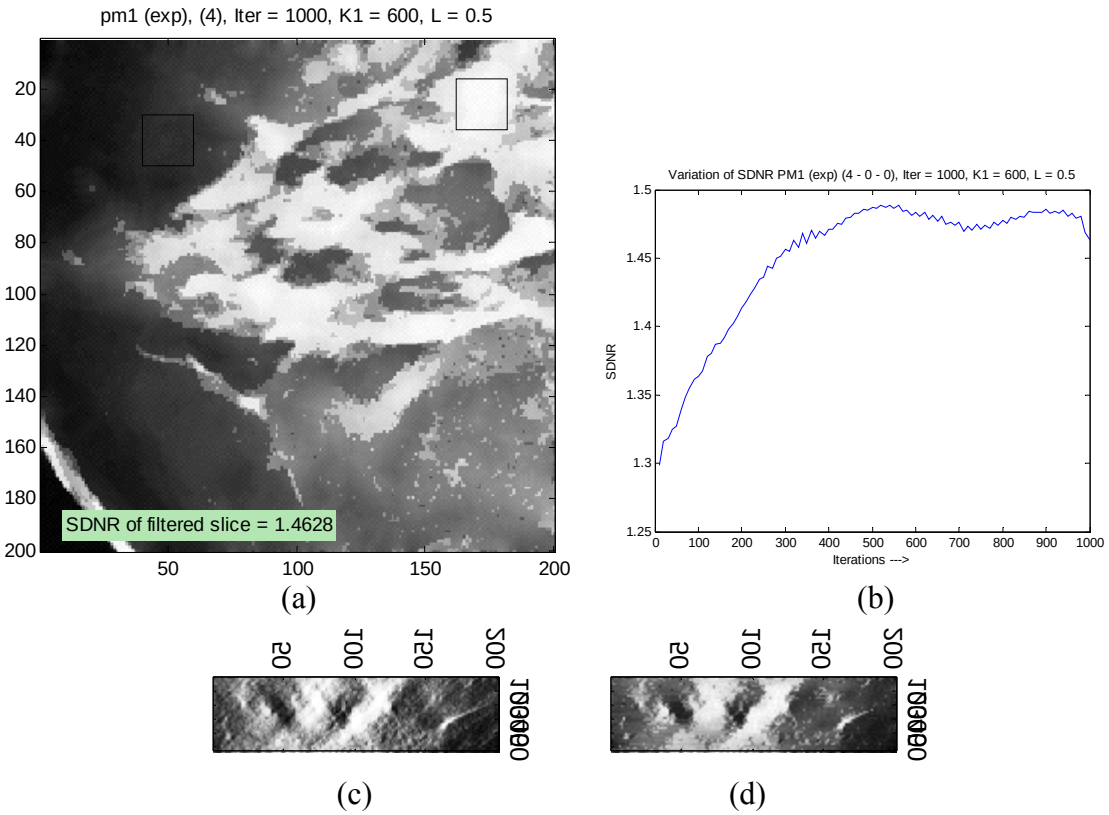

(a) (b)

(c) (d)

Figure 4.19: (a) Filtered Horizontal Slice (b) Variation of SDNR with Iterations (c) Original Vertical Slice (d) Filtered Image of the Original Vertical Slice Iterations = 500, L = 0.5, K = 600

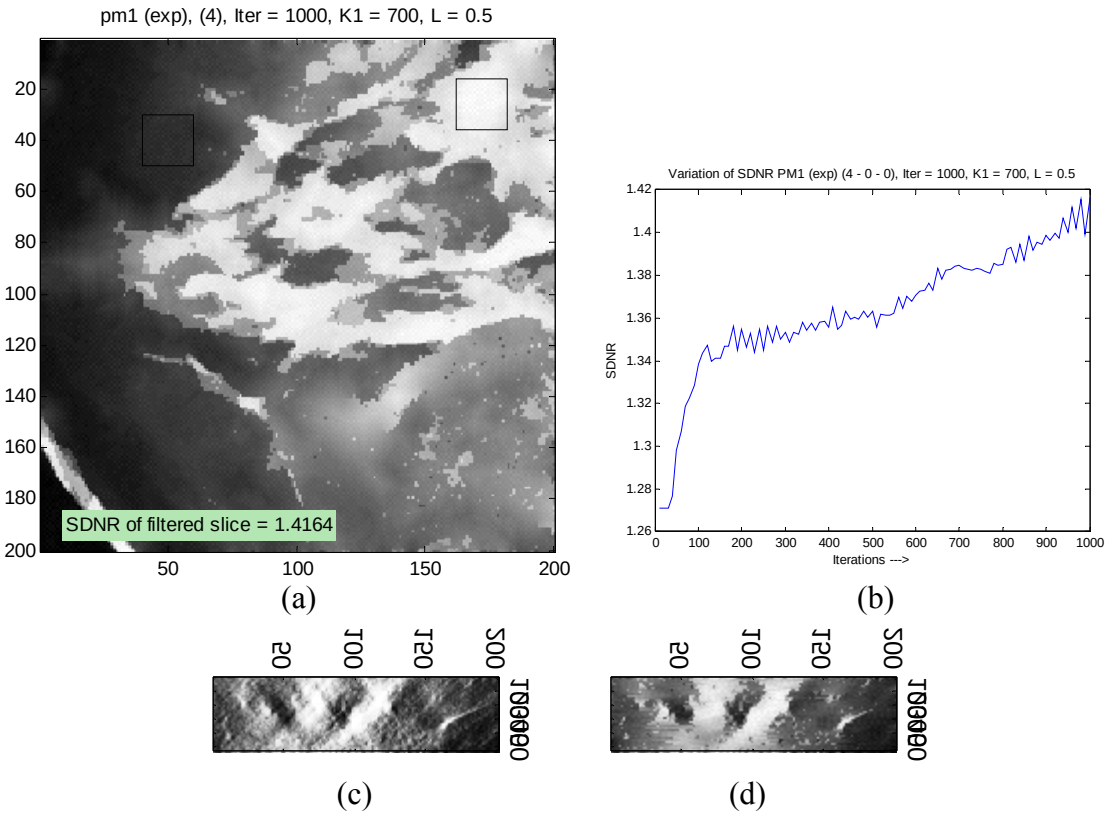

(a) (b)

(c) (d)

Figure 4.20: (a) Filtered Horizontal Slice (b) Variation of SDNR with Iterations (c) Original Vertical Slice (d) Filtered Image of the Original Vertical Slice Iterations = 500, L = 0.5, K = 700

A value for *K* of 500 yielded the largest SDNR. This result is displayed in Figure 4.18. An additional check was performed, during the investigation of the optimum value for *K*, by constructing a histogram of the variation of the SDNR with respect to a variation in *K*. The results are presented in Figure 4.21.

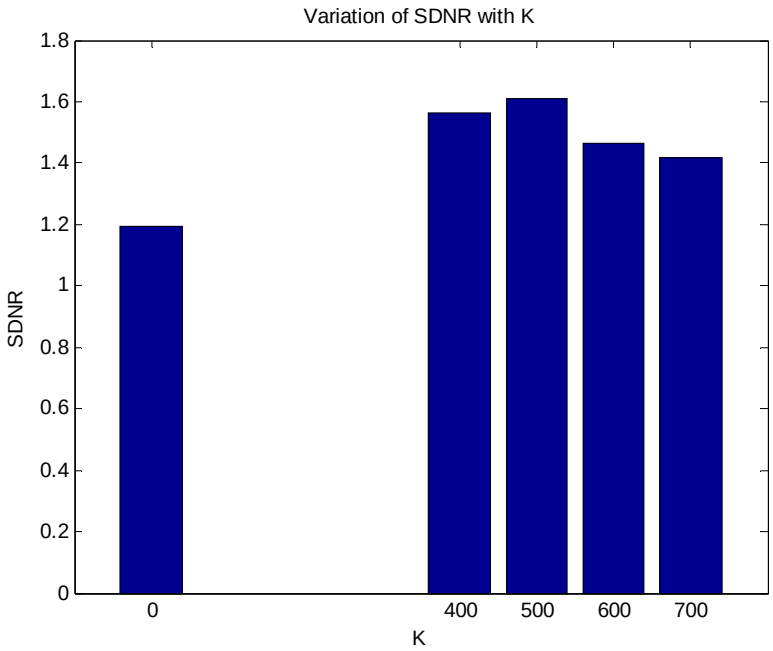

Figure 4.21: Variation of SDNR with Variation of K

Qualitatively the optimum value for *K* was found in Figure 4.18 to be 500. Quantitatively the highest SDNR was achieved for K = 500 as displayed in Figure 4.21. Additionally, qualitatively the out-of-plane artifacts were best eliminated for K = 500 for both in-plane and in-depth images.

4.2.3 2D Diffusion

In the 2D diffusion case, only pixels in the in-plane direction are considered during the filtering process. Two different windows, which consisted of 4 and 8 adjacent pixels, were considered for comparison. These 2D windows are depicted in Figure 4.22.

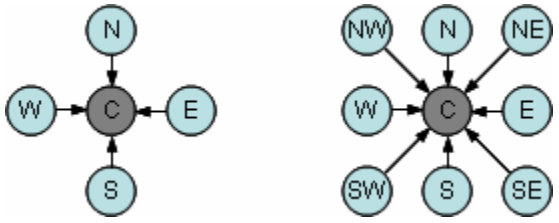

(a) (b)

Figure 4.22: (a) 4 Adjacent Pixels (b) 8 Adjacent Pixels

Pixels from the north, south, east and west directions were considered in the 4 adjacent pixels window. Pixels from northeast, northwest, southeast and southwest directions were considered in the 8 adjacent pixels window. An ROI was chosen for the 4 and 8 adjacent pixel analysis comparison. In each case the region was filtered with PM diffusion and the normalized line profile constructed.

The results of the analysis for the window containing 4 adjacent pixels are presented in Figures 4.23 and 4.24. Figure 4.23 presents the images before and after filtering and the associated line profiles.

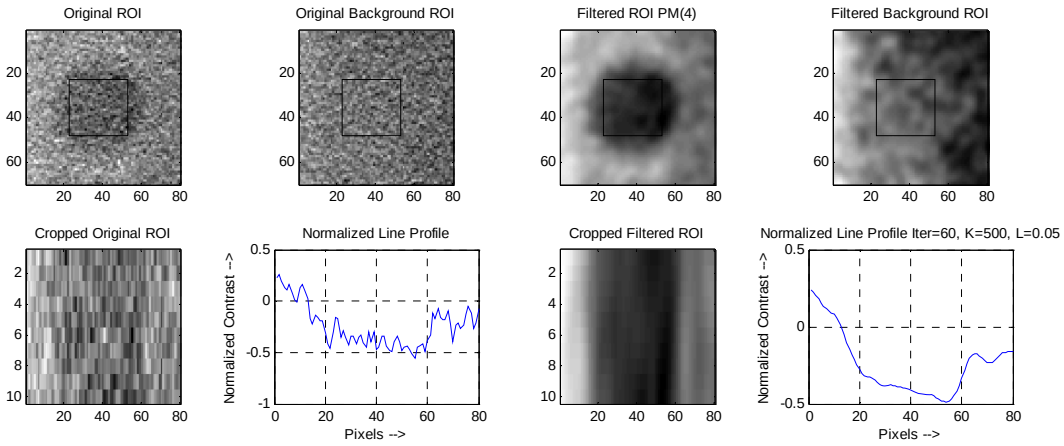

(a) (b)

Figure 4.23: (a) Original ROI (b) Filtered ROI with 4 point PM Diffusion

Figure 4.24 presents the data, in a comparison format, for the normalized original and filtered line profiles. The smoothing effect of the PM diffusion is clearly displayed in Figure 4.24.

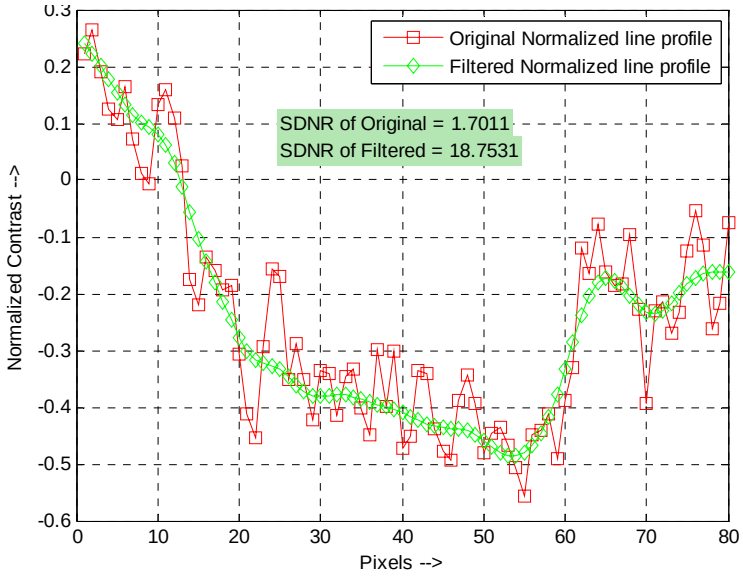

Figure 4.24: Normalized Line Profile for 4 Point PM Diffusion

The results of the analysis for the window containing 8 adjacent pixels are presented in Figures 4.25 and 4.26. Figure 4.25 only presents the images after filtering and the associated line profiles since the ROI did not change.

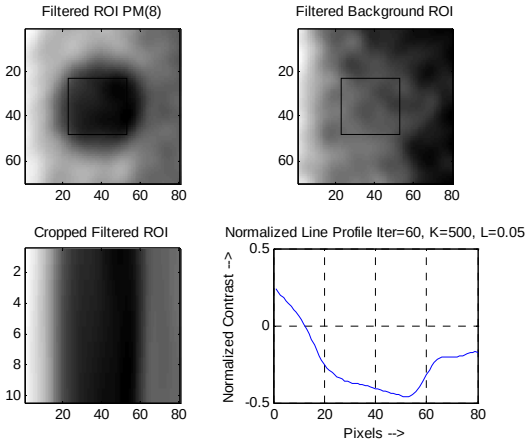

Figure 4.25: Filtered ROI with 8 Point PM Diffusion

Figure 4.26 presents the data, in a comparison format, for the normalized original and filtered line profiles for the window containing 8 adjacent pixels. The smoothing effect of the PM diffusion is clearly displayed in Figure 4.26.

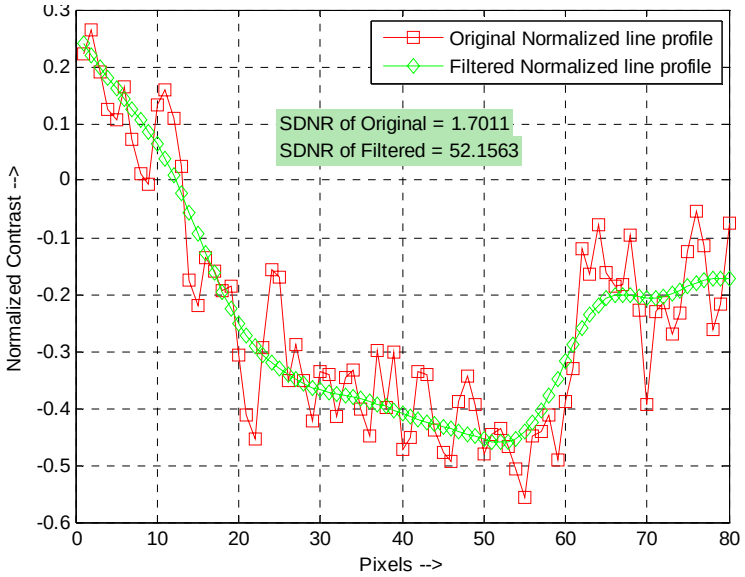

Figure 4.26: Normalized Line Profile for 8 Point PM Diffusion

A comparison of the SDNRs achieved as a function of the number of iterations is for the 4 and 8 adjacent pixel windows is presented in Figure 4.27.

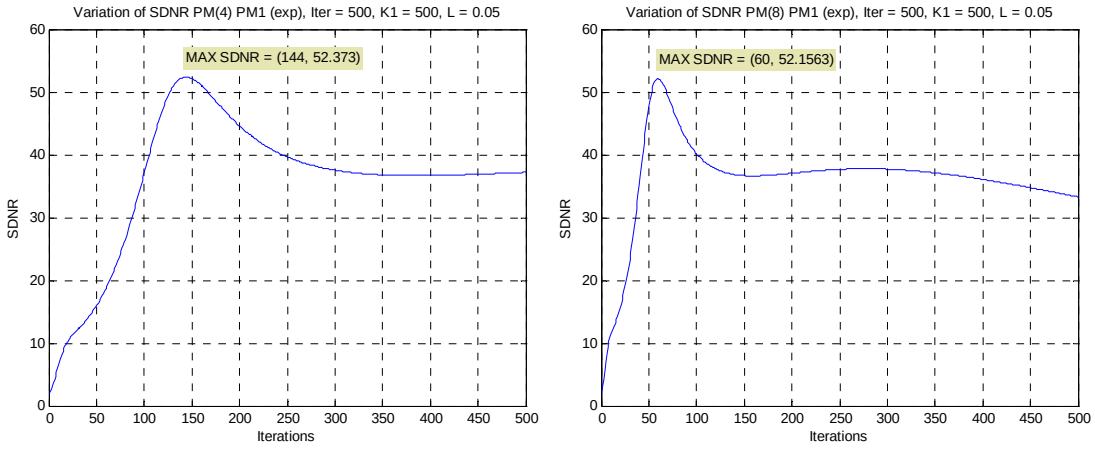

(a) (b)

Figure 4.27: Quantitative Difference for PM Diffusion Using
(a) 4 Adjacent Pixels (b) 8 Adjacent Pixels

Figure 4.27 demonstrates the relative similarity of the SDNR for both windows. The maximum SDNR achieved for the PM diffusion of the window containing 4 adjacent pixels occurred later than the highest SDNR achieved for the PM diffusion of the window containing 8 adjacent pixels. Therefore, the 8 adjacent pixel window was used to achieve a faster PM diffusion solution.

4.2.4 3D Diffusion

Instead of only considering pixels in the in-plane direction, pixels from the in-depth direction were also used in the filtering process. Diagrams for pixel selection involving in-plane and in-plane combined with in-depth pixels are presented in Figure 4.28.

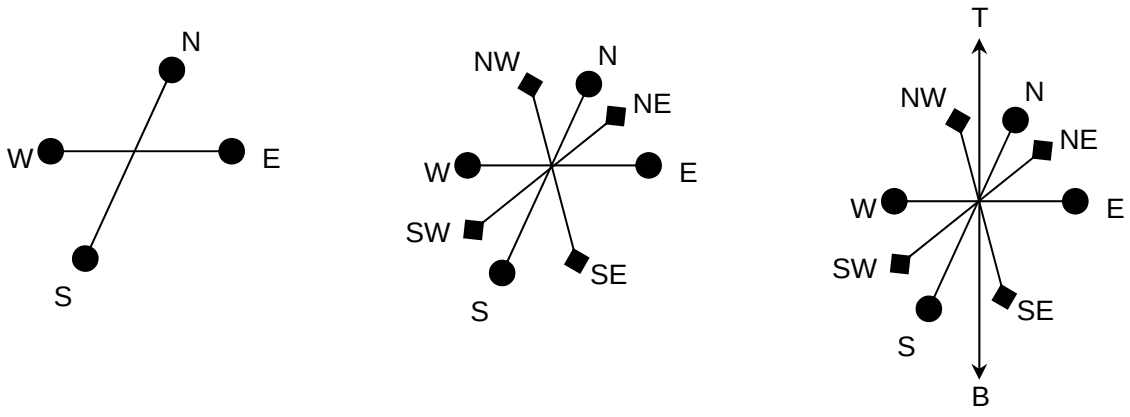

(a) (b) (c)

Figure 4.28: (a) 4 In-Plane Pixels (b) 8 In-Plane Pixels
(c) 8 In-Plane Pixels and 2 In-Depth Pixels

Four different windows were compared. Two of the windows were 2D based, ([4,0,0], [8,0,0]). The other two were 3D based, ([4,2,2], [8,2,2]). The horizontal slice, vertical slice and the variation of the SDNR with iterations are presented for each

window considered in Figures 4.29 – 4.32. The extracted vertical slice was 200x52, where 52 equals the number of slices. The value for K was chosen to be 500 and the learning coefficient was chosen to be 0.5 in order to achieve a faster solution.

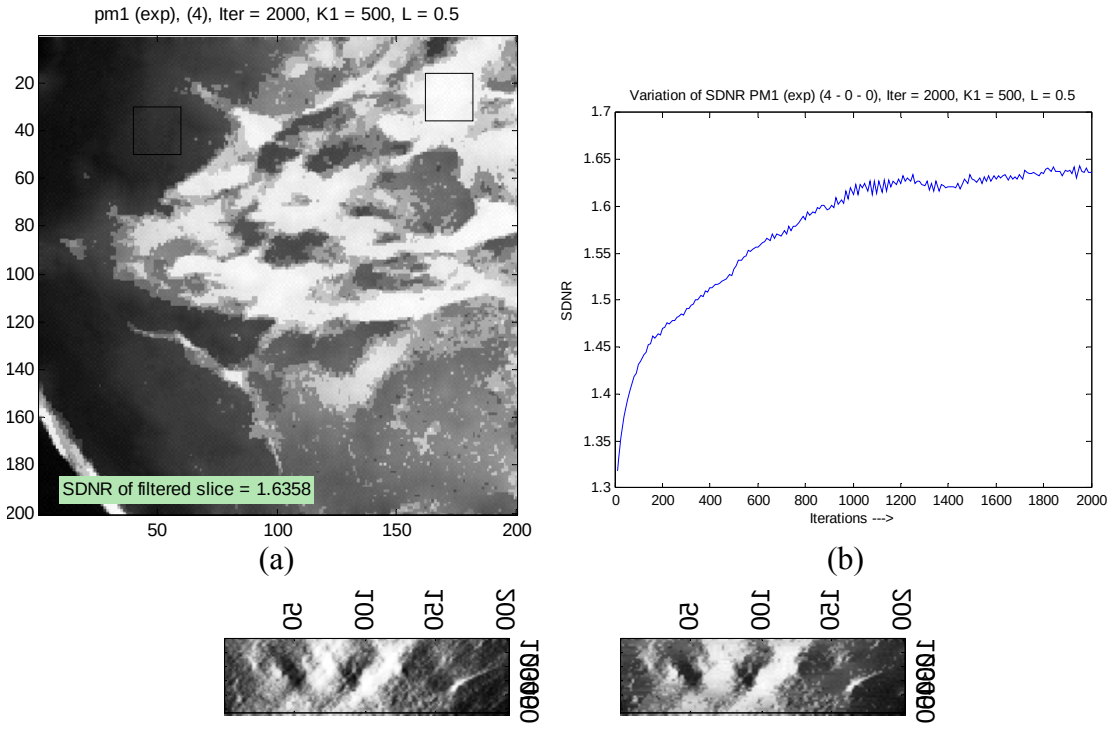

Figure 4.29: (a) Filtered Horizontal Slice (b) Variation of the SDNR with Iterations (c) Original Vertical Slice (d) Filtered Image of the Original Vertical Slice 2D, [4, 0, 0], Window

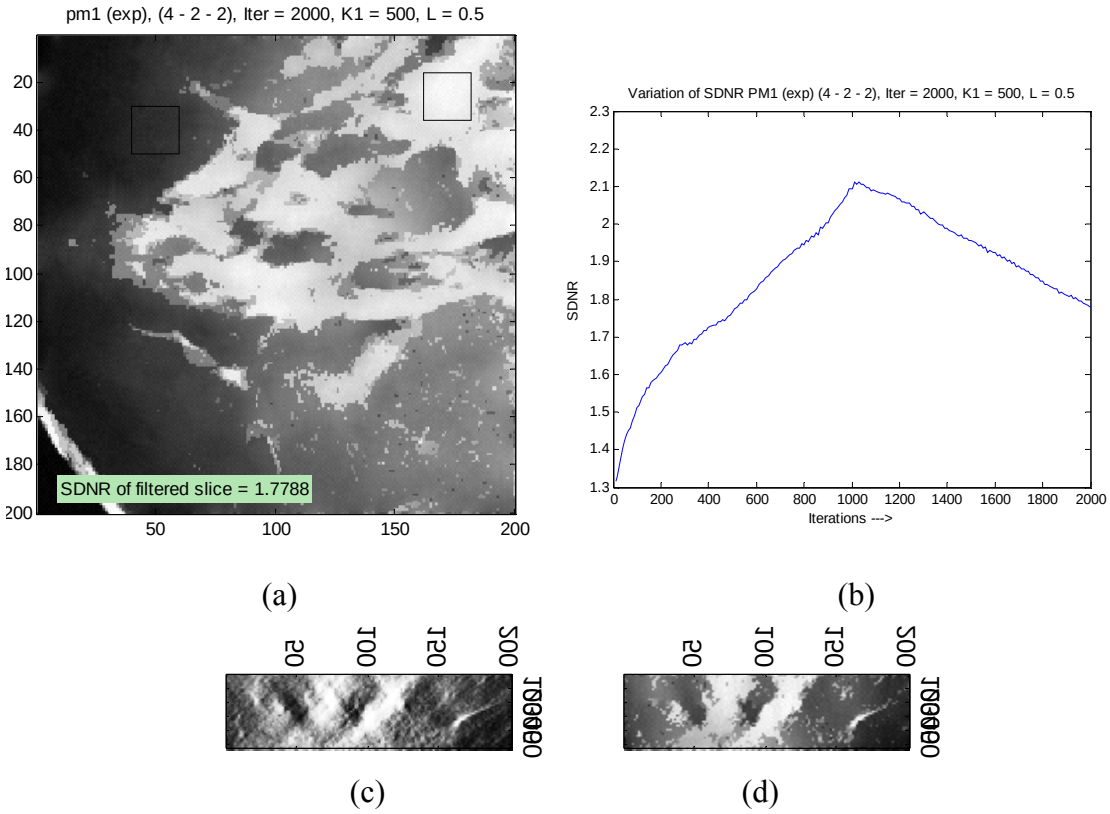

(a) (b)

(c) (d)

Figure 4.30: (a) Filtered Horizontal Slice (b) Variation of the SDNR with Iterations (c) Original Vertical Slice (d) Filtered Image of the Original Vertical Slice 2D, [4, 2, 2], Window

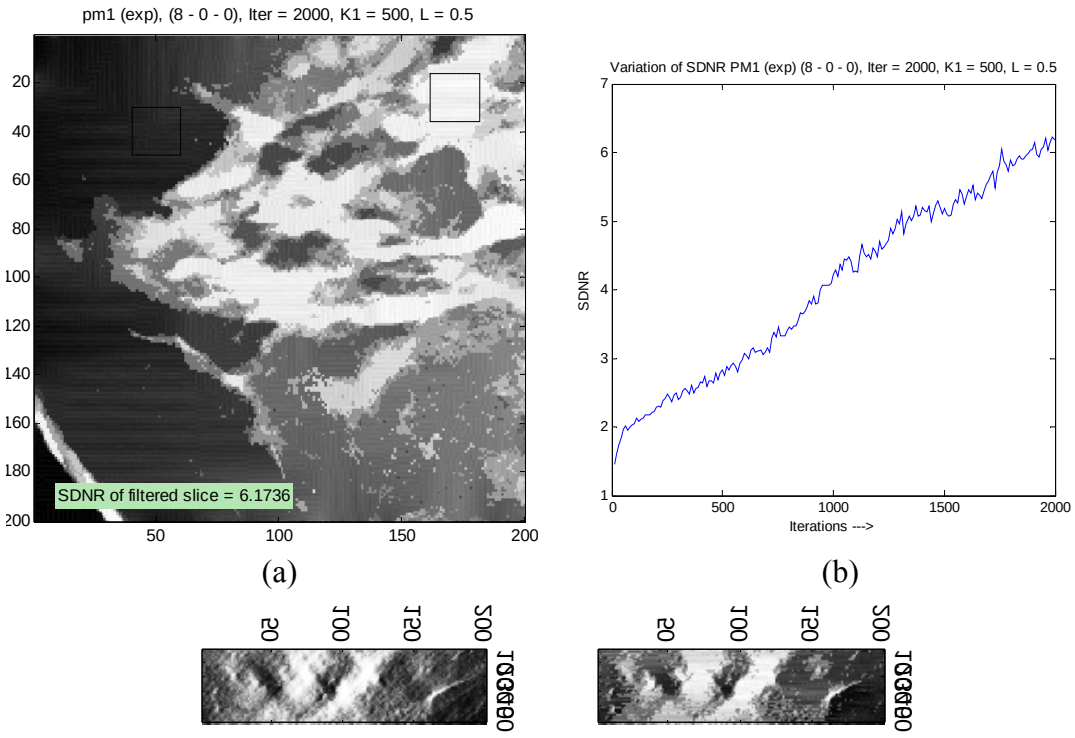

(a) (b)

(c) (d)

Figure 4.31: (a) Filtered Horizontal Slice (b) Variation of the SDNR with Iterations (c) Original Vertical Slice (d) Filtered Image of the Original Vertical Slice 3D, [8, 0, 0], Window

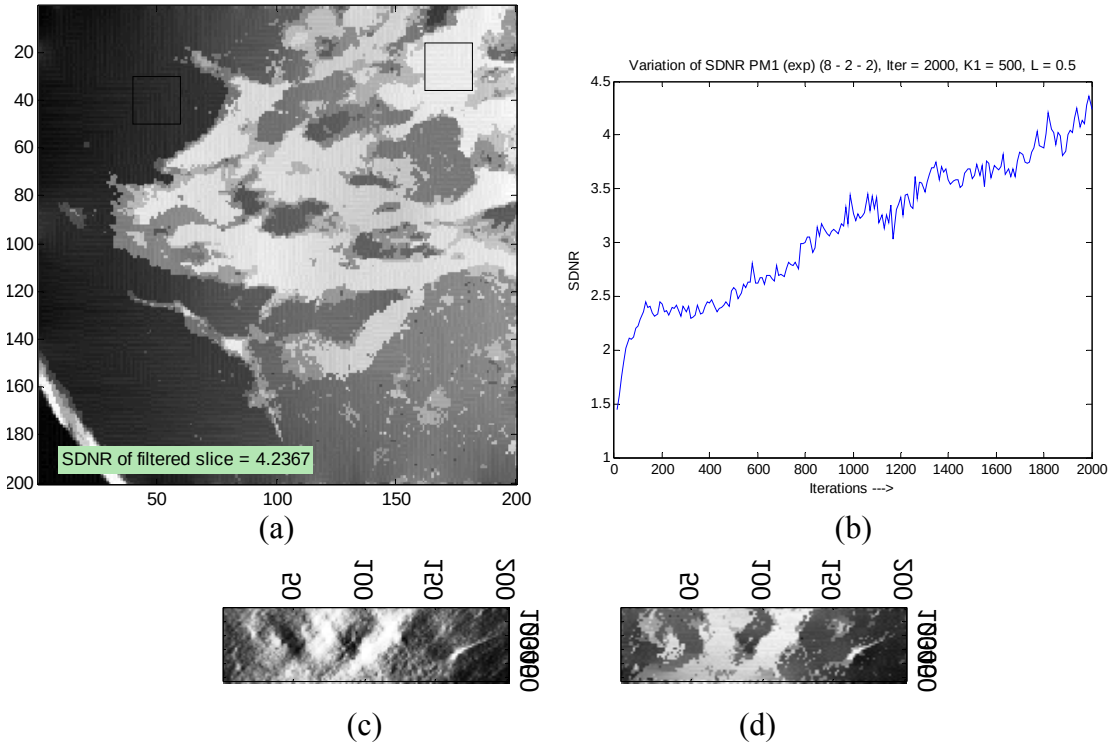

(a) (b)

(c) (d)

Figure 4.32: (a) Filtered Horizontal Slice (b) Variation of the SDNR with Iterations (c) Original Vertical Slice (d) Filtered Image of the Original Vertical Slice 3D, [8, 2, 2], Window

The data from the four windows, clearly indicates that the [4, 2, 2] window yielded the best results with respect to removal of out-of-plane artifacts. In addition, it is also clear that the in-plane SDNR for the [4, 2, 2] window was less than the in-plane SDNR for the [8, 0, 0] or [8, 2, 2] windows. The SDNR only provides image quality along the in-plane direction rather than the in-depth direction. However, the main objective of the anisotropic diffusion was removal of out-of-plane artifacts. Therefore, the [4, 2, 2] window was chosen as the proper window for the filtering.

CHAPTER 5

SEGMENTATION

After image pre-processing the next important step is detection of suspicious regions. Lesions associated with a tomosynthetic image appear more isolated than they would in a comparable mammographic image. This phenomenon is the result of less overlaying of the parenchyma tissue in the tomosynthesis procedure. Segmentation of suspicious regions is achieved through clustering, which consists of a procedure for finding a structure within the unlabelled data.

5.1 Clustering

Clustering is defined as finding a structure in unlabelled data, [Tutorial 2006]. Clustering is considered to be an unsupervised problem since the process lacks any a priori input. Clustering is also defined as a collection of objects, which can be placed, according to their correspondence to a descriptive concept, into groups or clusters. There is no absolute measure, which can be applied to determine the best clustering method. The best measure will vary as a function of the criteria established by the specific need to design a clustering procedure. Therefore, the effectiveness of the clustering method depends on the definition created by the criterion. The different types of clustering algorithms are:

- Exclusive clustering,
- Overlapping clustering,
- Hierarchical clustering,
- Probabilistic clustering.

5.2 Fuzzy Clustering

Developed by Dunn in 1973 and modified by Bezdek in 1981, fuzzy clustering is a very popular overlapping clustering algorithm. Fuzzy clustering is used extensively for image segmentation in medical field due to the sensitivity associated with assigning each data value to different clusters with closely associated degrees of sensitivity.

An image can be represented in various feature spaces. The FCM algorithm classifies the image by grouping similar data points in the feature domain into clusters. The clustering is achieved iteratively by maximizing the cost function that is dependent on the distance of the pixels to the clusters centers in the feature domain, [Chuang 2006]. Figure 5.1 presents a flow chart for the FCM algorithm.

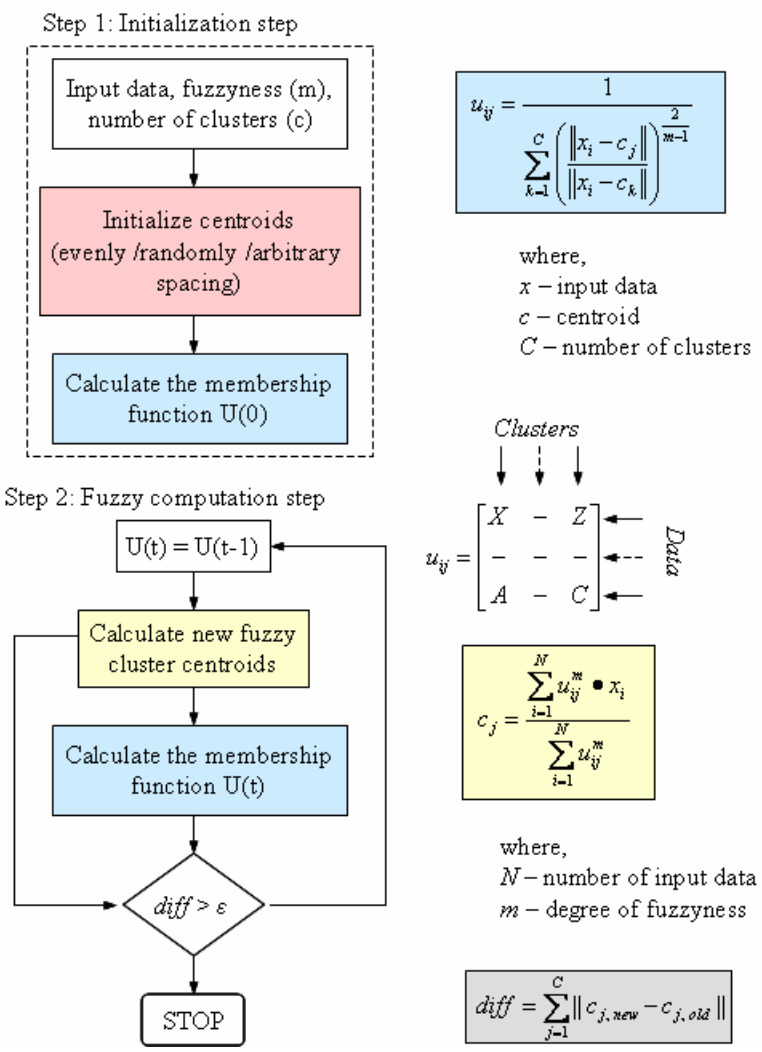

Figure 5.1: Flow Chart of the Fuzzy C-Means Clustering Algorithm

Figure 5.2(a) presents an unfiltered tomosynthesis image of an in-plane slice. Images (b), (c) and (d) present the results of the application of the FCM algorithm for three clusters. The lesion of interest lies in the southeast region at approximate horizontal and vertical coordinates of (165, 170). The presence, configuration and extent of the lesion has been dramatically enhanced by the application of the FCM algorithm.

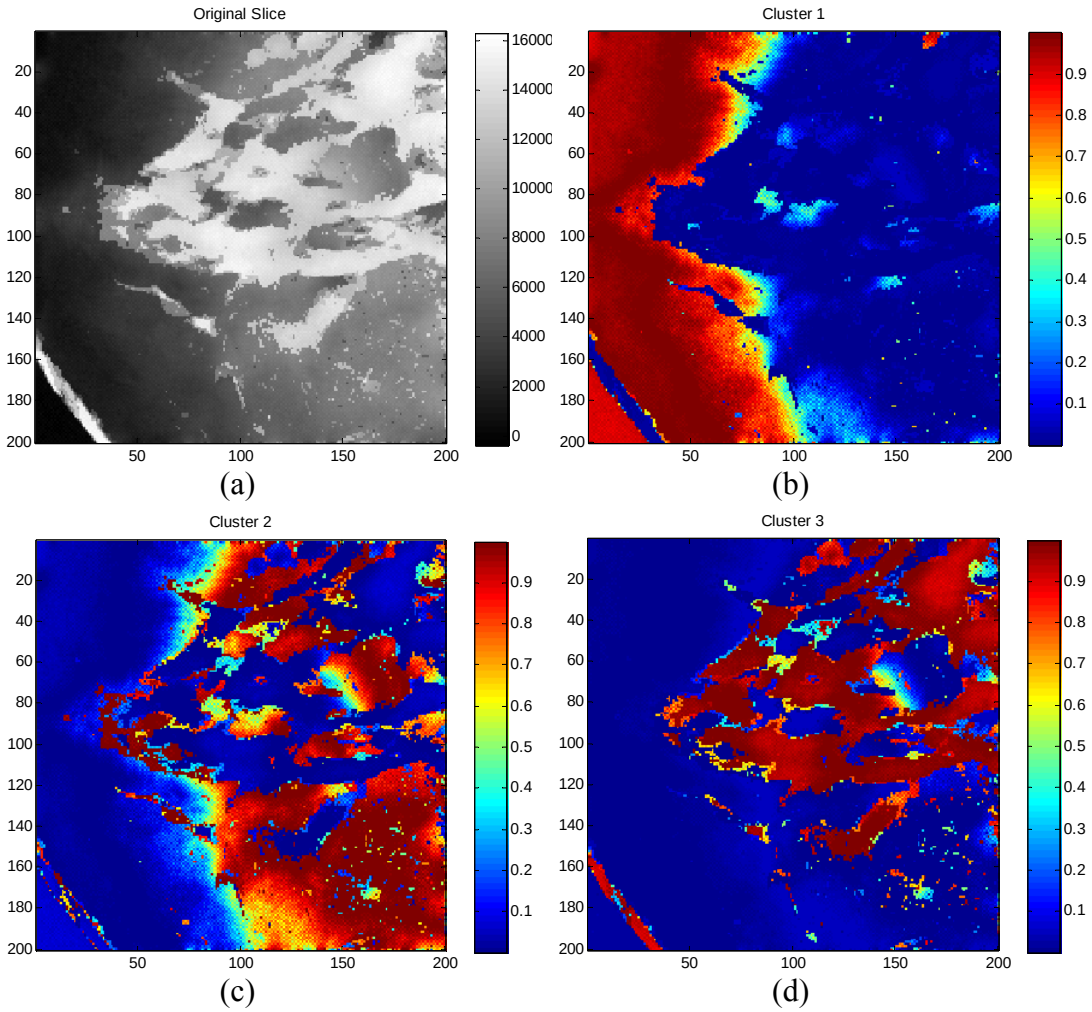

Figure 5.2: FCM of the Tomosynthesis Volume for 3 Clusters
(a) In-Plane Tomosynthesis Slice (b) Cluster 1
(c) Cluster 2 (d) Cluster 3

Figure 5.3 presents a segmentation of the same in-plane slice presented in Figure 5.2. It is clear that segmentation, by itself, does not provide the results that are possible with filtering and provides another example of the need for filtering.

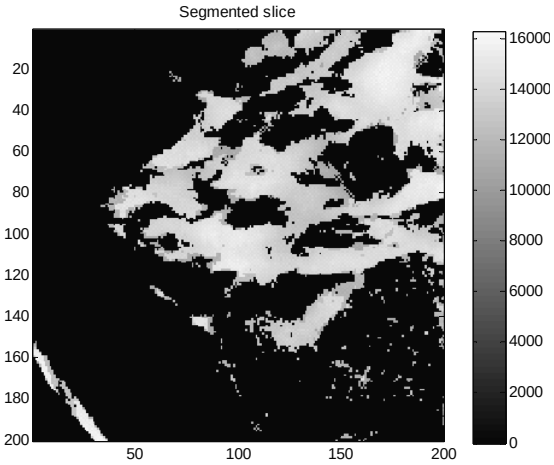

Figure 5.3: Segmented Tomosynthesis Volume for an In-Plane Slice

5.3 Cluster Validity Functions

Cluster validity functions are used to evaluate the performance of clustering. There are two important types of validity functions, [Wang 2004]. One type is based on the fuzzy partition of the sample set and the other type is based on the geometric structure of the sample set.

The functions representing the validity functions based on a fuzzy partition are labeled V_{pc} and V_{pe}. Less fuzziness of the partition indicates better performance. The validity functions for a fuzzy partition are defined by:

$$V_{pc} = \frac{\sum_{j=1}^{n} \sum_{i=1}^{c} u_{ij}^2}{n} \tag{1}$$

$$V_{pe} = -\frac{1}{n}\left[\sum_{j=1}^{n} \sum_{i=1}^{c} \left[u_{ij} \log u_{ij}\right]\right] \tag{2}$$

The optimal partition should generate a maximum for V_{pc} and a minimum for V_{pe}. The geometric structure of the sample set indicates that the samples within a particular cluster should exhibit more compactness and samples within different clusters should be separate. The functions representing the validity functions based on a geometric partition are labeled V_{fs} and $V_{xb,}$ [Xie 1991]. The validity functions for a geometric partition are defined by:

$$V_{fs} = \sum_{i=1}^{c} \sum_{j=1}^{n} u_{ij}^{2} \left(\left\| X_j - v_i \right\|^2 - \left\| v_i - \bar{v} \right\|^2 \right) \tag{3}$$

$$V_{xb} = \frac{\sum_{i=1}^{c} \sum_{j=1}^{n} u_{ij}^{2} \left\| X_j - v_i \right\|^2}{n * \left(\min_{i \neq k} \left\{ \left\| v_i - v_k \right\|^2 \right\} \right)} \tag{4}$$

Minimum values for V_{fs} and V_{xb} infer good clustering.

5.4 Spatial Fuzzy C-means Clustering

A conventional FCM algorithm does not fully utilize the spatial information in the image. SFCM incorporates spatial information into the objective function for clustering. The advantages of SFCM over conventional FCM are reduction of spurious blobs, noisy spots are removed and the procedure is less sensitive to noise. [Chuang 2006].

The pixels on an image are highly correlated, which means that the pixels in the immediate neighborhood possess nearly the same feature data. Therefore, the spatial

relationship of neighboring pixels is an important characteristic that can be of considerable aid in image segmentation.

The standard FCM procedure, wrongly classifies a noisy pixel due to its abnormal feature data. The SFCM technique incorporates spatial information and the membership weighing of each cluster is altered after the cluster distribution in the neighborhood is considered. The SFCM reduces the effect of noise considerably and biases the algorithm toward homogeneous clustering. Figure 5.4 presents the functions related to SFCM.

Spatial function

$$h_{ij} = \sum_{k \in NB(x_i)} u_{kj}$$

where, $NB(x_i)$ represents a square window centered on pixel x_i

Spatial function incorporated into membership function

$$u'_{ij} = \frac{u_{ij}^{p}\ h_{ij}^{q}}{\sum_{k=1}^{c} u_{ik}^{p}\ h_{ik}^{q}}$$

Figure 5.4: Spatial Function of the SFCM

The spatial function is given by:

$$h_{ij} = \sum_{k \in NB(x_i)} u_{kj}$$

where $NB(x_j)$ represents a square window centered on pixel x_j in the spatial domain. The spatial function h_{ij} represents the probability that the pixel x_j belong to i^{th} cluster. The spatial function of a pixel, for a cluster, is large if the majority of its neighborhood

belongs to the same cluster. The spatial function is incorporated into the membership function as:

$$u'_{ij} = \frac{u_{ij}^{p}\, h_{ij}^{q}}{\sum_{k=1}^{c} u_{ik}^{p}\, h_{ik}^{q}}$$

where p and q are parameters used to control the relative importance of both the membership functions. In a homogeneous region, the spatial function adds extra strength to the membership function and the clustering result remains unchanged. In the case of a noisy pixel, the spatial function reduces the weighting of a noisy cluster by the labels of its neighborhood pixels. Therefore, misclassified pixels from noisy regions or spurious blobs can be easily corrected.

The SFCM algorithm consists of a two-pass process during each iteration. The first pass is the same as the conventional FCM algorithm in order to calculate the membership function in the feature domain. During the second pass, the membership information of each pixel is mapped to the spectral domain and the spatial function is computed. The SFCM algorithm proceeds with the new membership that is incorporated by the spatial function.

5.5 Qualitative Analysis

Domain knowledge of the tomosynthetic data is used to calculate the number of clusters. Three cases are considered with 3, 4 and 5 numbers of clusters. It can be inferred from Figure 5.6 that after 4 clusters the increase in the numbers of clusters does

not contribute to the enhancement of the presence of the lesion. In fact, the increase to five clusters degraded the capability to definitively define the presence of the lesion

Case #1: Number of clusters = 3

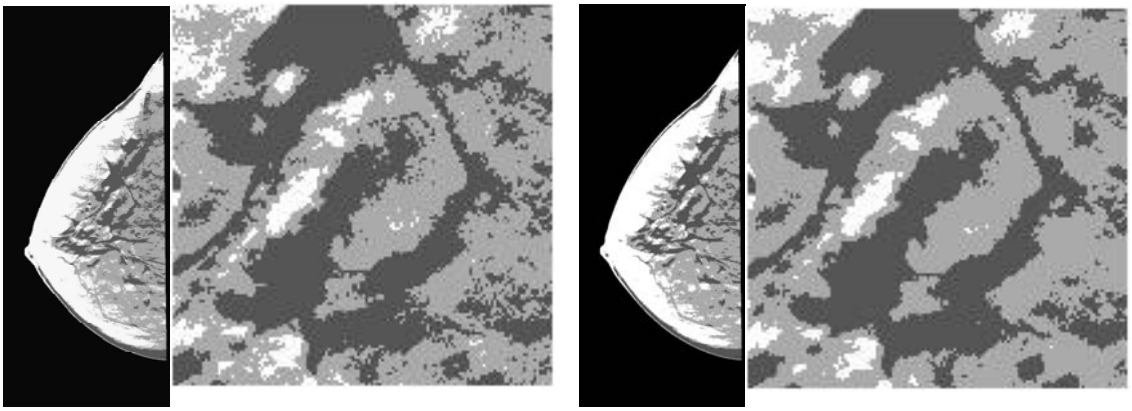

(a) (b)

Figure 5.5: (a) FCM (b) SFCM with a 5x5 Window Where $p = 1$, $q = 1$ and Clusters = 3

Case #2: Number of clusters = 4

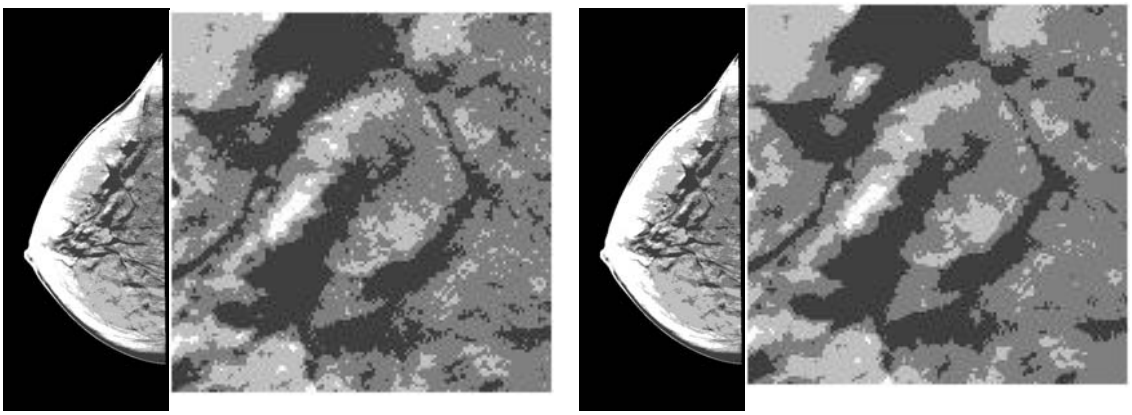

(a) (b)

Figure 5.6: (a) FCM (b) SFCM with a 5x5 Window Where $p = 1$, $q = 1$ and Clusters = 4

Case #3: Number of clusters = 5

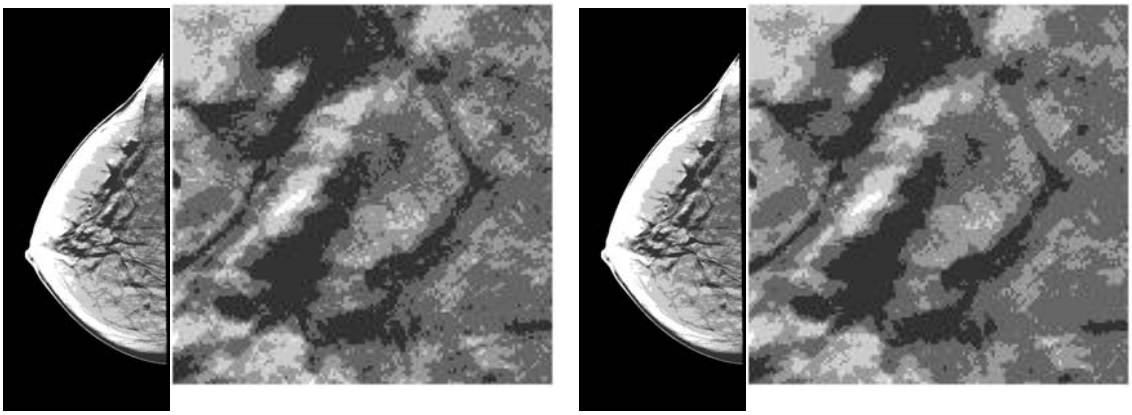

(a) (b)

Figure 5.7: (a) FCM (b) SFCM with a 5x5 Window Where $p = 1$, $q = 1$ and Clusters = 5

3D clustering involves the use of a 3D window in case of SFCM. Two windows, with dimensions of 5x5x3 and 5x5x5 were used to perform the qualitative comparison. The 5x5x5 window was less sensitive to out-of-plane artifacts when compared to the 5x5x3 window. Hence the 5x5x5 window was the window used for the SFCM algorithm. Figure 5.8 presents the results of the 3D clustering experiment for different window sizes.

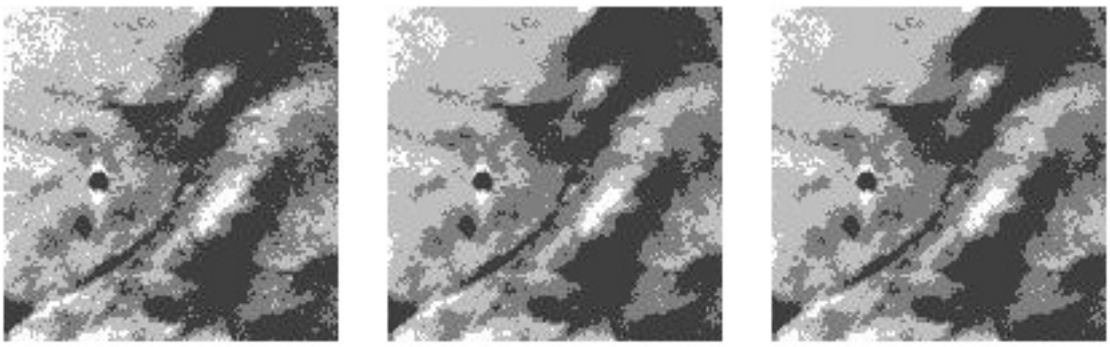

(a) (b) (c)

Figure 5.8: 3D Clustering of a Single Slice
(a) FCM (b) SFCM with a 5x5x3 Window
(c) SFCM with a 5x5x5 Window

A comparison between fuzzy and spatial fuzzy clustering of the original volume and the filtered volume are presented in Figures 5.9 and 5.10.

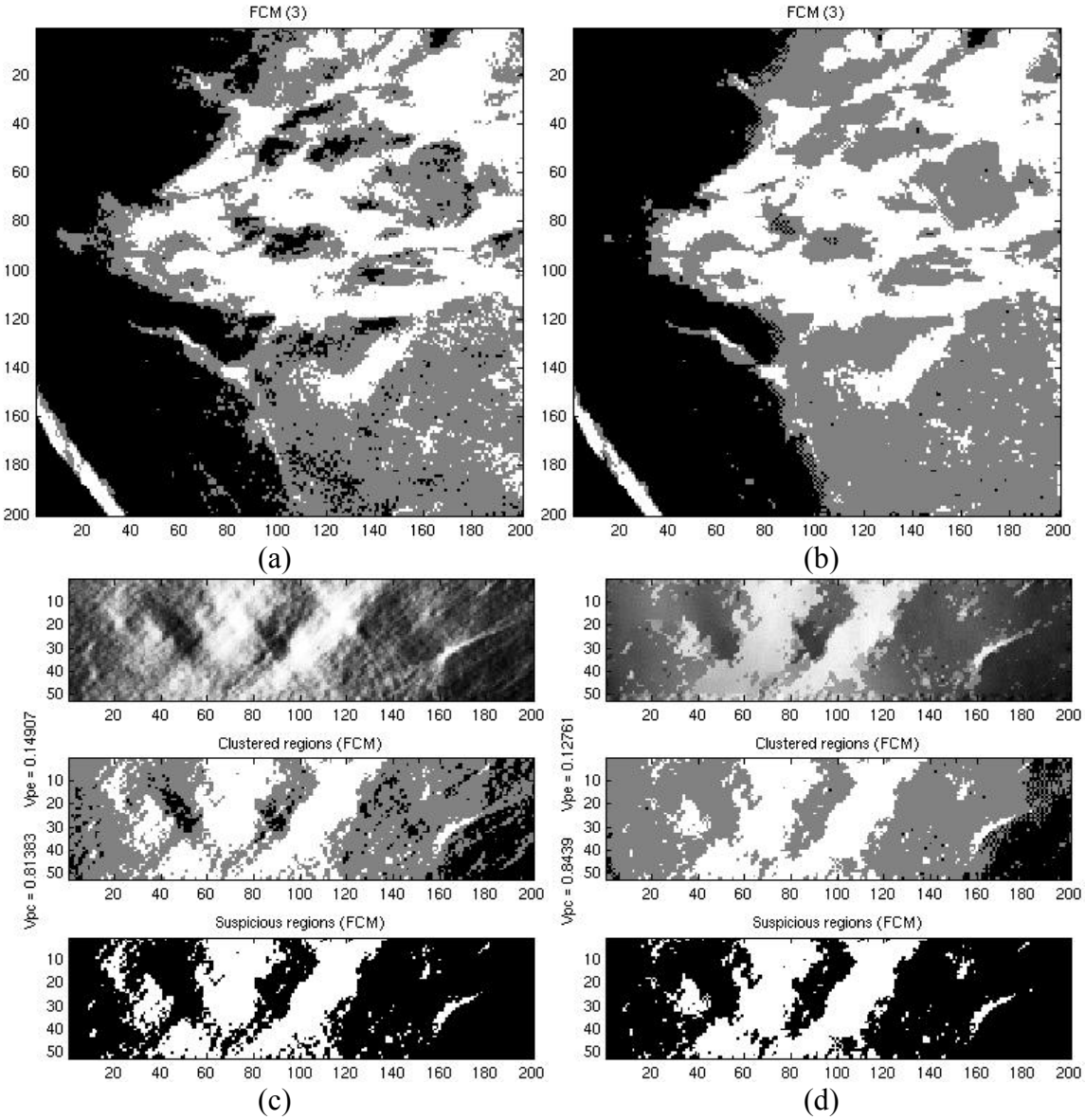

Figure 5.9: (a) FCM Clustered In-Plane Slice
(b) Filtered FCM Clustered In-Plane Slice
(c) Slice Along the In-Depth Direction of (a)
(d) Slice Along the In-Depth Direction of (b)

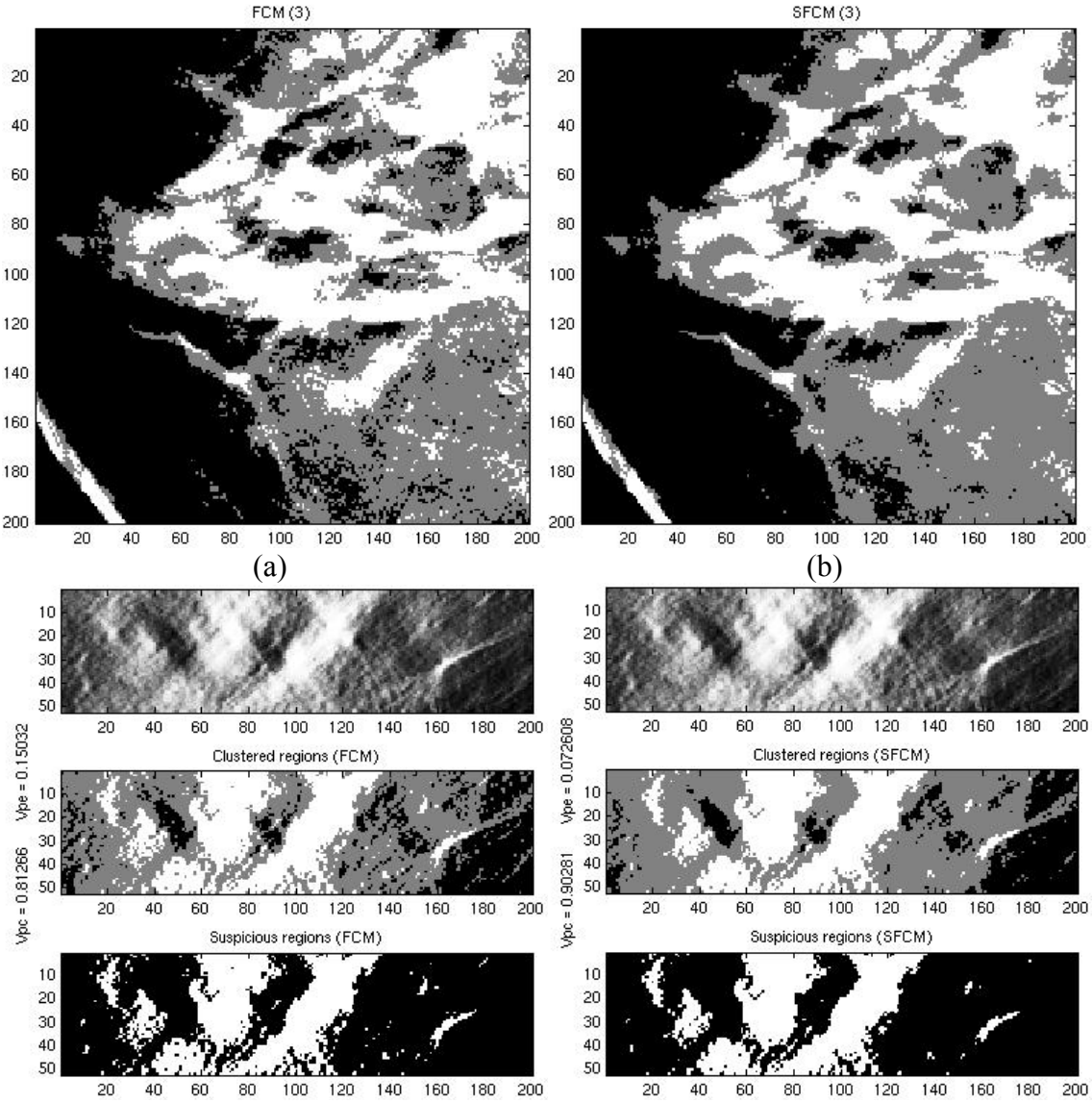

Figure 5.10: (a) FCM Clustered In-Plane Slice
(b) Filtered SFCM Clustered In-Plane Slice
(c) Slice Along the In-Depth Direction of (a)
(d) Slice Along the In-Depth Direction of (b)

The SFCM algorithm provided a better classification when compared to the FCM algorithm for both the original volume and the filtered volume.

5.6 Quantitative Analysis

The validity functions V_{pc} and V_{pe} were used to evaluate the performance difference between the FCM and the SFCM algorithms for 26 slices. The SFCM algorithm utilized a 5x5x5 window size. Table 5.1 presents the data for the validity functions associated with fuzzy and geometric clustering for the FCM and the SFCM algorithms. The data are consistent with the theory. The data demonstrate the superiority of the SFCM algorithm over the FCM algorithm.

Table 5.1: Variation of the Validity Functions with the Number of Clusters and the Type of Clustering

Number of Clusters		V_{pc}		V_{pe}		V_{xb}	
		With b/g	Without b/g	With b/g	Without b/g	With b/g	Without b/g
3	FCM	0.97361	0.90005	0.01942	0.07357	0.01688	0.02111
3	SFCM	0.98294	0.93537	0.01211	0.04586	0.01858	0.02327
4	FCM	0.97162	0.89249	0.02116	0.08017	0.01672	0.01576
4	SFCM	0.98122	0.92885	0.01337	0.05065	0.18842	0.17772
5	FCM	0.97053	0.88884	0.02214	0.08388	0.01669	0.01261
5	SFCM	0.97973	0.9232	0.01448	0.05485	0.01891	0.01429

Figure 5.11 presents a graphical comparison of the validity functions. The functions were compared on both original and filtered slices and for both algorithms. The results are consistent with theory and confirm the superiority of the SFCM algorithm over the FCM algorithm. The results presented in Figure 5.11 correspond to the presence of background effects in the left graphs and the absence of background effects in the right graphs for each validity function presented. Table 5.1 data and the graphs of Figure 5.11

indicate a distortion in the Vxb validity function since it should provide the least minimums when compared to Vpe. The SFCM algorithm works on the spatial domain. Therefore, the compactness of the clusters in the feature domain get distorted, which results in an abnormal variation of Vxb for both the FCM and SFCM algorithms.

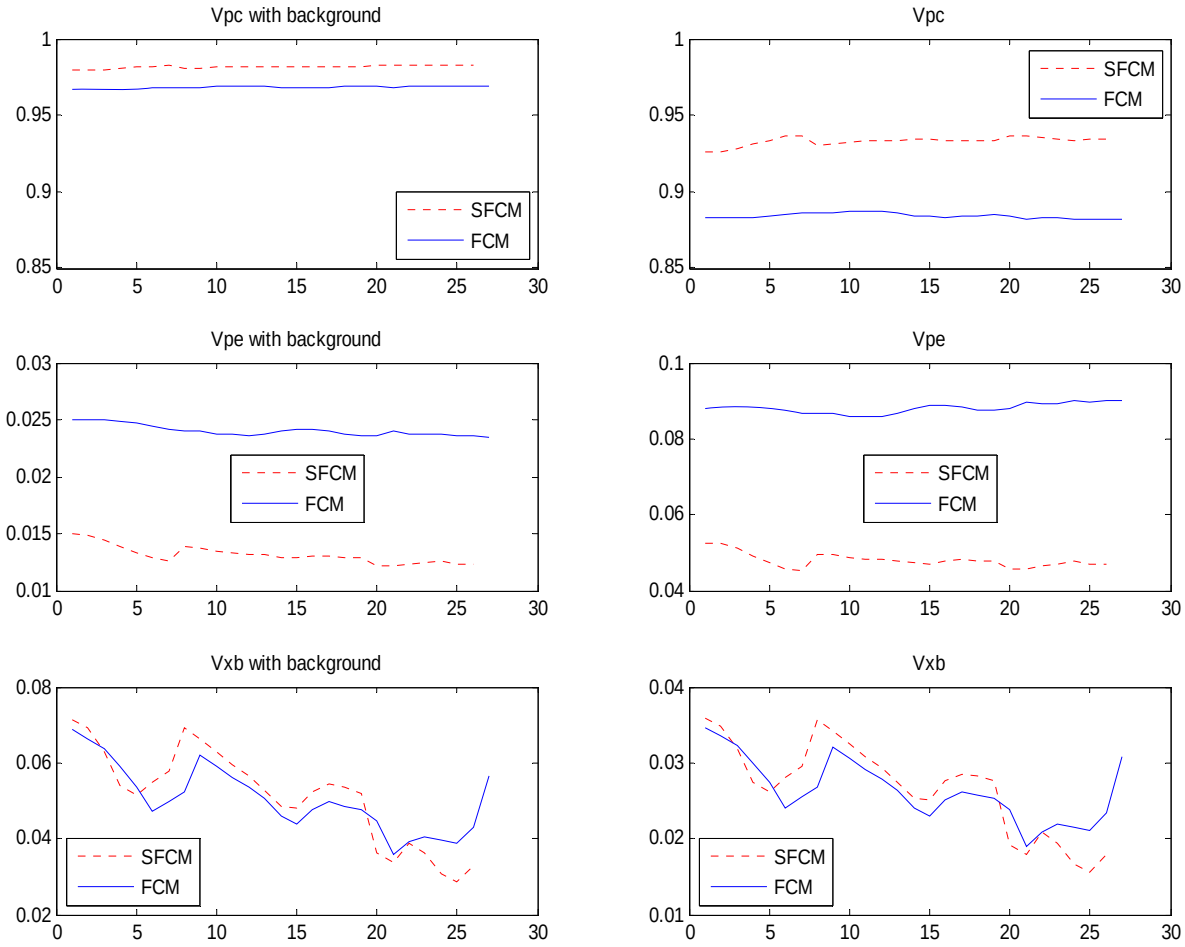

Figure 5.11: 2D Comparison Between FCM and SFCM for 26 Slices

A quantitative histogram comparison of the validity function for fuzzy clustering is presented in Figure 5.12. The histogram also demonstrates the superiority of the spatial fuzzy clustering of filtered volume over spatial fuzzy clustering of unfiltered and fuzzy clustering of filtered and unfiltered volumes.

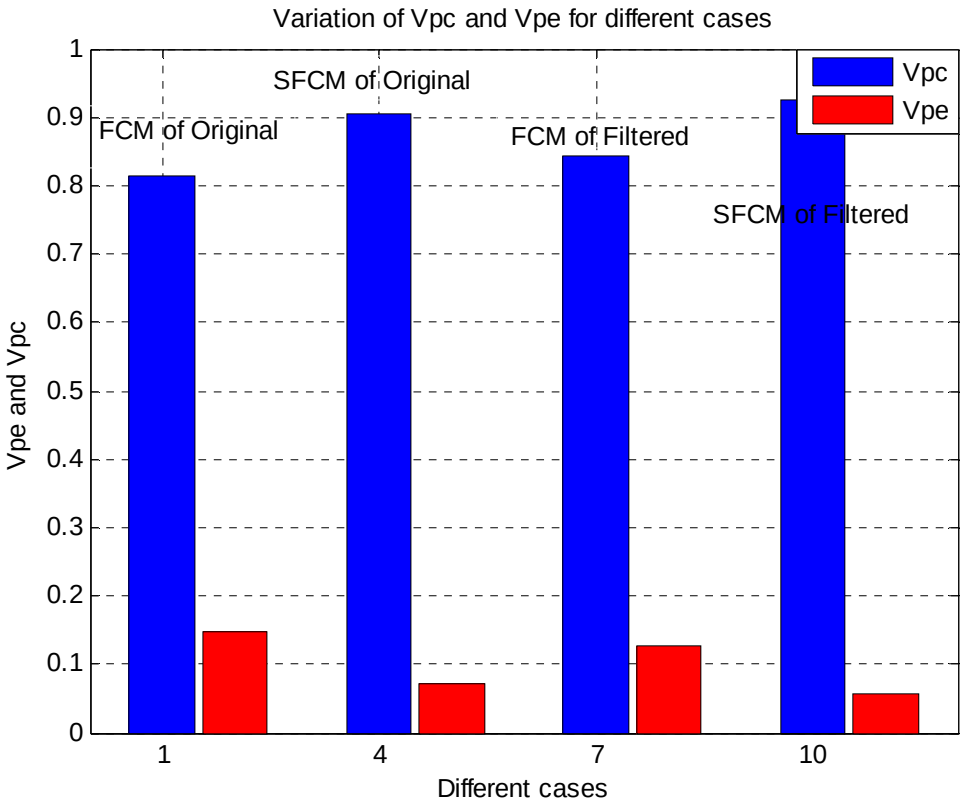

Figure 5.12: Variation Validity Functions Vpc and Vpe for SFCM and FCM Algorithms

CHAPTER 6

CONCLUSIONS AND RECOMMENDATIONS

6.1 Conclusions

Image pre-processing was performed to remove the background region and unwanted artifacts, which occur during image acquisition. The segmented breast volume was inversed and the histogram equalized in order to improve the contrast and to effectively use the available dynamic range of the image. Filtering, required values to be established for two critical parameters K and λ. The K and λ parameters are unique to tomosynthesis data and were calculated using phantom tomosynthesis and breast tomosynthesis volumes. The SDNR and line profiles were used to derive an effective conclusion for both the parameters. 2D anisotropic diffusion was implemented with different windows in order to determine an optimum window for in-plane filtering. Similarly, 3D anisotropic diffusion was used with different windows to remove the out-of-plane artifacts and increase the SDNR parameter.

Fuzzy C-means and Spatial Fuzzy C-means clustering methods were implemented in order to segment the suspicious regions. When employing the Spatial FCM algorithm, the anisotropic nature of the tomosynthetic data was included by modifying the multiplying parameter of the window, which was used. Comparison between the FCM and the SFCM algorithms was performed qualitatively using the visual representation of tomosynthesis horizontal and vertical slices and quantitatively using validity functions

such as the partition coefficient, the partition entropy and the Xie - Beni functions. In addition, a comparison of clustering between filtered and non-filtered tomosynthesis volumes was presented.

6.2 Recommendations

Classification of suspicious region by extending the 2D BIRADS system for 3D volumetric tomosynthesis data will be the next critical module for computer aided diagnosis of breast cancer. Application of contemporary pattern recognition algorithms, such as the support vector machine, (SVM), to enhance procedures that differentiate between abnormal breast lesions and normal breast tissues and further classify the abnormal objects as malignant or benign lesions should prove to be extremely beneficial. The essential requirement for a good classification analysis is a huge database. Therefore, acquiring data will play an important role in the success of diagnostic analysis. Since the existing module, which was the object of this research, was tested on a small database, it needs to be enhanced and, possibly, modified for a huge database set in order to be confidently used as a versatile tool for diagnosis.

The existing evaluation methods for good classification techniques are ROC and FROC curves which are based on 2D data. They need to be modified for analysis of 3D tomosynthesis classification.

REFERENCES

[ACS 2006], American Cancer Society, 2006

[Albagi 1997], Albagi, M.C. DeJule, P.F. Fitzgerald, D. F. Fobare, B. W. Giambattista, R.F. Kwasnick, J. Liu, S.J. Lubowski, G.E. Possin, J.F. Richotte, C. Wei and R. F. Wirth, "Digital Tomosynthesis in Breast Imaging", Radiology 1997, vol. 205, pp 399-406

[Albayrak 2003], Songul Albayrak and Fatih Amasyali, "Fuzzy C-Means Clustering on Medical Diagnostic Systems", International XII, Turkish Symposium on Artificial Intelligence and Neural Networks, TAINN

[Badea 1998] Cristian Badea, Zoi Kolitsi and Nicolas Pallikarakis, "A Wavlet-based Method for Removal of Out-of-Plane Structures in Digital Tomosynthesis," Computerized Medical Imaging and Graphics 22, pp 309-315

[BIRADS 1998], "Breast Imaging Reporting and Data System", third edition, American College of Radiology

[Brown 1995], Brown M.L., Houn F., Sickles E.A. and Kessler L.G., "Screening Mammography in Community Practice: Positive Predictive Value of Abnormal Findings and Yield of Follow-up Diagnostic Procedures", AJR Am. J. Roentgenol, vol. 165, pp 1373-1377

[CDC 2005], http://www.cdc.gov/nchs/hus.htm - Health_US_2005.pdf

[CFF 2006], "Cancer Facts & Figures", America Cancer Society

[Chakraborty 1984], Dev P. Chakraborty, Michael V. Yester, Gary T. Barnes and Arasanipalai V. Lakminarayanan, "Self-Masking Subtraction Tomosynthesis", Radiology vol. 150, pp 225-229

[Chan 2005], Heang-Ping Chan, Jun Wei, Elizabeth A. Rafferty, Tao Wu, Marilyn A. Roubidoux, Richard H. Moore, Daniel B. Kopans, Lubomir M. Hadjiiski and Mark A. Helvie, "Computer-aided Detection System for Breast Masses on Digital Tomosynthesis Mammograms: Preliminary Experience", Radiology vol. 237, pp 1075-1080

[Chen et al 2003], Zikuan Chen and Ruola Ning, "Why Should Breast Tumor Detection go Three Dimensional?", Phys. Med. Biol., vol. 48, pp 2217-2228

[Chuang 2006], Keh-Shih Chuang, Hong-Long Tzeng, Sharon Chen, Jay Wu and Tzong-Jer Chen, "Fuzzy C-means Clustering with Spatial Information for Image Segmentation", Computerized Medical Imaging and Graphics, vol. 30, pp 9-15

[Cunningham 1997], M. P. Cunningham, "The Breast Cancer Detection Demonstration Project 25 Years Later", A Cancer Journal for Clinicians, Vol. 47, Issue 3, pp 131-133

[DOBBINS 2003], James T Dobbins III, Devon J Godfrey, "Digital X-Ray Tomosythesis: Current State of the Art and Clinical Potential", Phys. Med. Biol., vol. 48, pp R65-R106

[Gerig 1992], Guido Gerig, Olaf Kubler, Ron Kikinis, and Ferenc A. Jolesz, "Nonlinear Anisotrpic Filtering of MRI Data", IEEE Transactions on Medical Imaging, vol. 11, pp. 221-232

[Hong 2004], Byung-Woo Hong, Matthew Mellor, Michael Brady and Stefano Soatto, "Combining Topological and Geometric Features of Mammograms to Detect Masses", Proc. Medical Image Understanding and Analysis, (MIUA), pp 196-199, London

[Imaginis 2006], http://imaginis.com/breasthealth/statistics.asp

[Kim 2005], J. Y. Kim, "Comparison of the Image Distortion Correction Methods for an X-Ray Digital Tomosynthesis System", ICIAR 2005, LNCS 3656, pp. 286-293, 2005

[Kolitsi 1993], Z. Kolitsi, G. Panayiotakis and N. Pallikarakis, "A Method for Selective Removal of Out-of-Plane Structures in Digital Tomosynthesis", Med. Phys, 20(1)

[Mushlin 1998], Mushlin A.I., Kouides R.W. and Shaprio D.E., "Estimating the Accuracy of Screening Mammography: A Meta-Analysis", Am. J. Prev. Med, vol. 14, pp 143-153

[Niklason 1997], L T Niklason, B T Christian, L E Niklason, D B Kopans, D E Castleberry, B H Opsabl-Ong, C E Landberg, P J Slanetz, A A Giardino, R Moore, D Albagi, M C DeJule, P F Fitzgerald, D F Fobare, B W Giambattista, R F Kwasnick, J Liu, S J Lubowski, G E Possin, J F Richotte, C Wei, R Fwirth, "Digital Tomosynthesis in Breast Imaging", Radiology 1997; vol. 205, pp 399-406

[Parallax 2006], http://en.wikipedia.org/wiki/Parallax

[Qian et al., 1993], Qian W., Kallergi M. and Clarke L.P., "Order Statistic-Neural Network Hybrid Filters for Gamma Camera Image Restoration", IEEE Trans. in Medical Imaging, vol. 12(1), pp 56-65

[Qian et al., 1994a], Qian W., Clarke L.P., Kallergi M., Clark R.A., "Tree-Structured Nonlinear Filters in Digital Mammography", IEEE Trans. Med. Imag., vol. 13(1), pp 25-36

[Qian et al., 1994b], Qian W. and Clarke L.P., "Digital Mammography: M-channel Quadrature Mirror Filters for Micro-calcification Extraction", Computerized Imaging and Graphics, vol. 18(5), pp 301-314

[Qian et al., 1995a], Qian W., Kallergi M., Clarke L.P., Li H.D., Clark R.A. and Silbiger, M.L., "Tree-Structured Nonlinear Filter and Wavelet Transform for Micro-Calcification Segmentation in Digital Mammography", Med. Phys., vol. 22(8), pp 1247-1254

[Qian et al., 1995b], Qian W., Clarke L.P., Kallergi M., Zheng B. and Clark R.A., "Wavelet Transform for Computer Assisted Diagnosis, (CAD), for Digital Mammography", IEEE Engineering in Medicine and Biology Magazine, (Invited Paper), vol. 14(5), pp 561-569

[Qian et al., 1995c], Qian W. and Clarke L.P., "Hybrid M-Channel Wavelet Transform Methods: Adaptive, Automatic and Digital X-Ray Sensor Independent", Medical Physics, vol. 22(6), pp 983-4

[Qian et al., 1996], Qian W. and Clarke L.P., "Wavelet-Based Neural Network with Fuzzy-Logic Adaptivity for Nuclear Image Restoration", Proceedings of the IEEE, Special Issue on Applications of Neural Networks, (invited paper), vol. 84(10)

[Qian et al., 1997], Qian W., Li L. and Clarke L.P., "Digital Mammography: Wavelet Based CAD Method for Mass Detection", Proc. of SPIE Medical Imaging

[Qian et al., 1998a], Qian W., Li L., Clarke L.P., Mao F. and Clark R.A., "Adaptive CAD Modules for Mass Detection in Digital Mammography", The Proceedings of 20th Annual Conference of the IEEE Engineering in Medicine and Biology Society, 1998

[Qian et al., 1998b], Qian W., "Digital Mammography: Hybrid 4-Channel Wavelet Transform for Microcalcification Segmentation", Academic Radiology, vol. 5(5), pp 354-365

[Qian et al., 1999a], Qian W., Li L. and Clarke L.P., "Image Feature Extraction for Mass Detection using Digital Mammography: Influence of Wavelet Analysis", Medical Physics, vol. 26(3), pp 402-408

[Qian et al., 1999b], Qian W. and Clarke L.P., "Digital Mammography: Comparison of Adaptive and Non-Adaptive CAD Methods for Mass Detection", Academic Radiology, vol. 6(8), pp 471-480

[Qian et al., 2000], Qian W., "A Novel Hybrid Filter Architecture for Image Enhancement in Medical Imaging", Handbook of Medical Image Processing, Vol. 2, Academic Press, 2000

[Qian et al., 2001], Qian W., Sun X.J., Song D.S. and Clark R.A., "Digital Mammography: Wavelet Transform and Kalman Filtering Neural Network in Mass Segmentation and Detection", Academic Radiology, vol. 8, pp 1074-1082

[Qian et al., 2002a], Qian W., Sun X.J. and Clark R.A., "Multi-Resolution/Multi-Orientation Based Nonlinear Filters for Image Enhancement and Detection in Digital Mammography", Journal of X-Ray Science and Technology, vol. 10(1-2), pp 1-15

[Qian et al., 2002b], Qian W., Mao F., Song D.S., Sun X.J. and Clark R.A., "An Improved Method of Region Grouping for Micro-Calcification Detection in Digital Mammograms", Computerized Medical Imaging and Graphics, vol. 26(6), pp 361-368

[Qian et al., 2003], Qian W., Zhang Y., Sun X.J., Song D.S. and Sankar R., "A New Computer-Aided Diagnosis System for Prostate Cancer Detection on TRUS Imaging", Proceedings of 9th IASTED International Conference on Signal and Image Processing, Honolulu, Hawaii

[Qian et al., 2004], Qian W., Song D.S., Zhou J., Sun X., Tockman M. and Sharma A., "Computer-Aided Pathological Diagnosis of Lung Cancer Cells", Submitted to the IEEE Trans. on Image Processing, Special Issue on Molecular and Cellular Bioimaging

[Qian et al., 2005], Qian W., Sankar R., Song X.S., Sun X.J. and Clark R.A., "Standardization for Image Characteristics in Telemammography using Genetic and Nonlinear Algorithms", Computers in Biology and Medicine, vol. 35(3), pp 183-196

[Roy 1985], D.N. Ghosh, Roy R.A., Kruger B., Yih, and P. Del Rio, "Selective Plane Removal in Limited Angle Tomographic Imaging", Med. Phys., vol. 12(1)

[Rozhkova 2000], N. I. Rozhkova, E. G. Chikirdin, Yu, G. Ryudiger, G. P. Kochetova, I. V. Lisachenko and O. E. Yakobs, "Hardware for Mammography", Biomedical Engineering, Vol. 34, No. 5, pp. 277-279. Translated from Meditsinskaya Tekhnika, Vol. 34, No. 5, pp. 45-47, 2000. Original article submitted January 27, 2000

[Russ 1995], John C Russ, "The Image Processing Handbook – Second Edition"

[Sharyl 2001], Sharyl J., Nass, I., Craig Henderson and Joyce C. Lashof, "Mammography and Beyond: Developing Technologies for the Early Detection of Breast Cancer", National Academy Press

[Sun et al., 2004], Xuejun Sun, Wei Qian and Dansheng Song, "Ipsilateral-Mammogram Computer-Aided Detection of Breast Cancer", Computerized Medical Imaging and Graphics, vol. 28, pp 151-158

[Suri 2002], Jasjit S., Suri, J.Gao, Sameer Singh and Swamy Laxminarayan, "A Comparision of Sate-of-the-Art Diffusion Imaging Techniques for Smoothing Medical/Non-Medical Image Data," ICPR, vol 1, pp 10508-10511

[Tutorial 2006], "A tutorial on Clustering Algorithms", http://www.elet.polimi.it/upload/matteucc/Clustering/tutorial_html/

[Voci 2004], Francesco Voci, Shigeru Eiho, Naozo Sugimoto and Hiroyuki Sekiguchi, "Estimating the Gradient Threshold in the Perona-Malik Equation", IEEE Signal Processing Magazine, pp. 39-46

[Wang 2004], Xizhao Wang, Yadong Wang and Lijuan Wang, "Improving Fuzzy C-Means Clustering Based on Feature-Weight Learning", Pattern Recognition Letters vol. 25, pp 1123 – 1132

[Wu 2003], T Wu, R Moore, E Rafferty, D Kopans, A Stewart, W Phillips, M Stanton, J Eberhard, B Opsahl-Ong, L Niklason and M Williams, "Tomosynthesis Mammography Reconstruction Using a Maximum Likelihood Method", Abstract, AAPM 45th Annual Meeting

[Wu 2004], Tao Wu, Richard H. Moore, Elizabeth A. Rafferty and Daniel B. Kopans, "A Comparison of Reconstruction Algorithms for Breast Tomosynthesis", Med. Phys., vol. 31(9)

[Xie 1991], Xuanli Lisa Xie and Gerardo Beni, "A Validity Measure for Fuzzy Clustering", IEEE Transactions on Pattern Analysis and Machine Intelligence, Vol. 13(8)

[Yankaskas 2001], Bonnie C. Yankaskas, Rebecca J. Cleveland, Michael J. Schell and Robert Kozar, "Association of Recall Rates with Sensitivity and Positive Predictive Values of Screening Mammography", American Journal of Roentgen Ray Society, vol. 177[3], pp 543-549

[Zhang 2004], Dao-Qiang Zhang and Song-Can Chen, "A Novel Kernelized Fuzzy C-Means Algorithm with Applications in Medical Image Segmentation", Artificial Intelligence in Medicine, vol. 32, pp 37-50

[UNITED STATES PATENT SCITED]
Qian W. United States Patent, No. 5576548, Nov.1996: "Nuclear Imaging Enhancer"

Qian W. United States Patent, No. 5799100, Aug. 1998: "Computer-Assisted Method and Apparatus for Analysis of X-Ray Images Using Wavelet Transforms"

Qian W. United States Patent, No. 5825936, Oct. 1998: "Image Analyzing Device Using Adaptive Criteria"

Qian W. United States Patent, No. 5987094, Nov. 1999: "Computer-Assisted Method and Apparatus for the Detection of Lung Nodules"

QianW. United States Patent, No. 5982917, Nov.1999: "Computer-Assisted Method and Apparatus for Displaying X-ray Images"